

# **Engineered Wnt ligands enable blood-brain barrier repair in neurological disorders**

## **Authors:**

Maud Martin<sup>1</sup>, Simon Vermeiren<sup>1</sup>, Naguissa Bostaille<sup>1</sup>, Marie Eubelen<sup>1</sup>, Daniel Spitzer<sup>2</sup>, Marjorie Vermeersch<sup>3</sup>, Caterina P. Profaci<sup>4</sup>, Elisa Pozuelo<sup>5</sup>, Xavier Toussay<sup>6</sup>, Joanna Raman-Nair<sup>6</sup>, Patricia Tebabi<sup>1</sup>, Michelle America<sup>1</sup>, Aurélie de Groot<sup>5</sup>, Leslie E. Sanderson<sup>1</sup>, Pauline Cabochette<sup>1</sup>, Raoul F.V. Germano<sup>1</sup>, David Torres<sup>7</sup>, Sébastien Boutry<sup>3</sup>, Alban de Kerchove d'Exaerde<sup>5</sup>, Eric Bellefroid<sup>8</sup>, Timothy N Phoenix<sup>9</sup>, Kavi Devraj<sup>2</sup>, Baptiste Lacoste<sup>6</sup>, Richard Daneman<sup>4</sup>, Stefan Liebner<sup>2</sup>, Benoit Vanhollebeke<sup>1,10,\*</sup>

## **Affiliations:**

<sup>1</sup> Laboratory of Neurovascular Signaling, Department of Molecular Biology, ULB Neuroscience Institute, Université libre de Bruxelles (ULB), Gosselies B-6041, Belgium

<sup>2</sup> Institute of Neurology (Edinger Institute), University Hospital, Goethe University Frankfurt, Frankfurt am Main, Germany

<sup>3</sup> Center for Microscopy and Molecular Imaging (CMMI), Université libre de Bruxelles (ULB), Université de Mons (UMONS), Gosselies B-6041, Belgium

<sup>4</sup> Departments of Pharmacology and Neurosciences, University of California, San Diego, La Jolla, CA, USA

<sup>5</sup> Laboratory of Neurophysiology, ULB Neuroscience Institute, Université libre de Bruxelles (ULB), Brussels B-1070, Belgium

<sup>6</sup> Ottawa Hospital Research Institute, Neuroscience Program, Department of Cellular and Molecular Medicine, University of Ottawa Brain and Mind Research Institute, Faculty of Medicine, Ottawa, ON, Canada

<sup>7</sup> Institut d'Immunologie Médicale, Université libre de Bruxelles (ULB), Gosselies, Belgium

<sup>8</sup> Laboratory of Developmental Genetics, ULB Neuroscience Institute, Université libre de Bruxelles (ULB), Gosselies B-6041, Belgium

<sup>9</sup> Division of Pharmaceutical Sciences, James L. Winkle College of Pharmacy, University of Cincinnati, Cincinnati, OH, USA

<sup>10</sup> Walloon Excellence in Life Sciences and Biotechnology (WELBIO), Belgium

\* Correspondence to: Benoit.Vanhollebeke@ulb.be

### **Abstract:**

The blood-brain barrier (BBB) safeguards the central nervous system (CNS) from harmful blood-borne factors. While BBB dysfunction is a hallmark of several neurological disorders, therapies to restore BBB function are lacking. An attractive strategy is to repurpose developmental BBB regulators, like Wnt7a, into BBB-protective agents. However, safe therapeutic use of Wnt ligands is complicated by their pleiotropic Frizzled signaling activities. Taking advantage of the Wnt7a/b-specific Gpr124/Reck co-receptor complex, we genetically engineered Wnt7a ligands into BBB-specific Wnt activators. In a hit-and-run AAV-assisted CNS gene delivery setting, these new Gpr124/Reck-specific agonists protected BBB function, thereby mitigating glioblastoma expansion and ischemic stroke infarction. This work reveals that the signaling specificity of Wnt ligands is adjustable and defines a novel modality to treat CNS disorders by normalizing the BBB.

**One sentence summary:** Repurposing Wnt7a ligands into BBB therapeutics

**Main text:**

Proper function of the central nervous system (CNS) requires a tightly controlled environment safeguarded from harmful blood-borne components and pathogens. This environment is maintained by the blood-brain barrier (BBB), a set of properties of CNS vascular endothelial cells (ECs). The BBB is induced and maintained by signals derived from other cells of the neurovascular unit (NVU), most notably pericytes and astrocytes (1–5). Within the healthy NVU, the endothelial monolayer limits paracellular permeability by linking adjacent cell membranes through tight junctions, represses transcellular traffic by downregulating vesicular transport, constrains immune cell trafficking, and uses ATP-fueled transporters to efflux a wide range of undesirable small molecules back into the bloodstream. This physiological barrier consequently only allows carefully selected blood constituents to enter the CNS parenchyma by engaging substrate-specific receptors and transporters at the endothelial BBB gate (1–5).

BBB dysfunction, along with varying degrees of cerebrovascular hyperpermeability, neurovascular uncoupling, or blood flow dysregulation, has been linked to stroke, gliomas, epilepsy, traumatic brain injury, and neurodegenerative disorders (1, 4, 6, 5, 7, 8). Upon BBB breakdown, leakage of neurotoxic plasma components, infiltration of immune cells, and CNS milieu alterations contribute to neuronal demise and worsen disease outcome (9, 5). However, despite their broad therapeutic potential across a wide range of disorders, clinically-approved BBB-protective strategies are currently lacking.

Among the many pathways that control neurovascular function, endothelial Wnt/ $\beta$ -catenin signaling acts as a master regulator of BBB physiology in response to neural-derived Wnt7a/b ligands. Wnt/ $\beta$ -catenin signaling initiates the BBB differentiation cascade at the earliest steps of CNS vascular invasion, and then maintains BBB function in adults (10–13). Recent evidence suggests that inhibition of Wnt signaling by conditional deletion of  $\beta$ -catenin signaling in ECs

causes BBB breakdown (10–15) and accelerates disease progression in stroke, glioblastoma, and multiple sclerosis in mice (16–18). Conversely, recombining a constitutively active form of  $\beta$ -catenin in the CNS endothelium is protective in models of brain cancer and stroke (16, 18). Hence, identifying safe modalities to enhance Wnt/ $\beta$ -catenin signaling selectively at the BBB constitutes a promising therapeutic avenue for a range of neurological disorders.

As Wnt7a/b are the endogenous ligands controlling  $\beta$ -catenin-dependent BBB maturation, they constitute, in principle, legitimate therapeutic agents to repair the dysfunctional BBB. However, Wnt signaling exerts pleiotropic functions across a range of tissues and organs, in both health and disease (19). More so, the structural modalities of Wnt/Frizzled (Fz) interactions *a priori* disqualify natural Wnt ligands as safe therapeutics. Wnt7a/b indeed belongs to a multigenic family of 19 closely related secreted glycoproteins that fold into an unusual two-domain structure reminiscent of a human hand (20). The N-terminal domain (NTD, **Fig. 1A**) exposes a palmitoleic acid moiety at its “thumb” extension, and the C-terminal domain (CTD, **Fig. 1A**) “index” is composed of hydrophobic residues. Wnt ligands bind to the ten members of the Fz family of receptors by pinching the globular cysteine-rich domain (CRD) of the receptors between their “thumb” (site 1) and “index” (site 2) (pale orange areas, **Fig. 1A**). Notably, the interaction chemistry involves conserved residues among both the ligand’s and the receptor’s multigenic families.

Consequently, the 19 Wnt ligands and their 10 Fz receptors interact promiscuously, with many Wnts able to engage a single Fz receptor, and multiple Fz receptors competing for any particular Wnt ligand. Delivering Wnt7a/b ligands *in vivo* is thus predicted to have multiple adverse outcomes, including altered organogenesis (21, 22), stem cell expansion (23, 24), and tumorigenesis (25, 26). Accordingly, Wnt7a overexpression is incompatible with proper vertebrate development: when expressed in *Xenopus* embryos, Wnt7a causes axis duplication,



a classical dysmorphic outcome of exacerbated Wnt/ $\beta$ -catenin signaling (**fig. S1A**). Similarly, Wnt7a and other “canonical” Wnt ligands induce posteriorization of the anterior nervous system in zebrafish embryos, resulting in the loss of forebrain and eye structures (**fig. S1B**). This promiscuous signaling mode, together with the widespread Frizzled expression patterns, and the difficulty in producing active Wnt proteins at bulk levels, has contributed to hampering the clinical development of Wnt-signaling based therapies.

Interestingly, cerebral ECs cell-autonomously resort to a highly atypical Wnt7a/b-specific receptor complex to activate Wnt/ $\beta$ -catenin signaling for brain angiogenesis and BBB regulation (27, 28). This receptor complex is composed of the GPI-anchored glycoprotein Reck and the adhesion G-protein coupled receptor Gpr124. Reck, after physically binding to the linker peptide of Wnt7a/b NTD (**Fig. 1A**, pink residues), stabilizes the ligand in a signaling-competent lipophilic conformation and delivers it to Fz receptors via the transmembrane tethering function of Gpr124. Thereby, Reck and Gpr124 synergistically stimulate Wnt7a/b-specific responses by assembling higher-order Gpr124/Reck/Fz/Lrp5/6 complexes (29–31).

Wnt7a/b thus activates two distinct types of membrane receptor complexes. One has broad tissue distribution and binds non-discriminately to Wnt7a/b and other Wnt ligands via two contacts sites within the Fz CRD, and a less well-known interaction with Lrp5/6 (**Fig. 1A**, hereafter termed systemic “off-target” complex). The other complex is enriched at the level of the BBB ECs and is highly specific for Wnt7a/b. In this case, Reck provides an additional contact point by binding at least in part to the divergent linker peptide of Wnt7a/b (**Fig 1A**, BBB “on-target”).

Taking advantage of the differential composition of these receptor complexes, we attempted to selectively target the BBB by engineering Wnt7a/b into Gpr124/Reck-specific agonists. To that end, we first established the genetic bases of Gpr124/Reck-dependent Wnt7a/b/Fz signaling.

We compared Wnt signaling induced by 17 Wnt ligands, including Wnt7a and Wnt7b, in pairwise combination with each of the ten Fz receptors in WT, *GPR124*<sup>-/-</sup>;*RECK*<sup>-/-</sup> and Gpr124/Reck-overexpressing Wnt/ $\beta$ -catenin reporting super top flash (STF) HEK293 cells (**fig. S2**). WT and *GPR124*<sup>-/-</sup>;*RECK*<sup>-/-</sup> cells revealed a near-identical Wnt/Fz signaling landscape with multiple Wnt ligands signaling through several Fz receptors and most Fz responding to multiple Wnt ligands, as anticipated from the poorly discriminative Wnt/Fz binding mechanism (20). Wnt7a and Wnt7b signaled preferentially through Fz5 and Fz8 in WT and *GPR124*<sup>-/-</sup>;*RECK*<sup>-/-</sup> cells (**fig. S2A, B, Table S1**). However, as reported previously (27), Wnt7a/b signals were selectively and potently stimulated upon Gpr124 and Reck over-expression even in the absence of a co-expressed Fz (**fig. S2C, Table S1**). This illustrates that the endogenous pool of Fz receptors is sufficient to support Wnt7a/b signaling in HEK cells (32, 33, 27). In order to determine which Fz isoform is competent for Gpr124/Reck-stimulated Wnt7a/b signaling, we knocked out *GPR124* and *RECK* in previously-generated *FZ1-10*<sup>-/-</sup> mutant cells by CRISPR/Cas9 mutagenesis (29). STF-based reporter assays in this 12 loci null genetic background allowed us to unambiguously test individual components by transient re-expression. This setting revealed that, albeit at different levels, most Fzs were competent for Wnt7a and Wnt7b upon expression of Reck and Gpr124, with Fz1, 4, 5, 8, and 9 exhibiting the highest potency (**Fig. 1A and fig. S3A**). On a cautionary note, the relative expression level or membrane localization of different Fz receptors was not assessed. In the absence of Gpr124/Reck, Fz5 and Fz8 were confirmed as the only Wnt7a or Wnt7b signaling receptors (**Fig. 1A and fig. S3B**).

The near-uniform competence of Fz isoforms for Gpr124/Reck-dependent Wnt7a signaling was unexpected (31) and reveals that Wnt7a/b loses its capacity to discriminate Fz receptors when bound by Reck within the Gpr124/Reck/Fz/Lrp5/6 complex. As Wnt ligands discriminate Fz receptors primarily *via* site 2 (20), we suspected that Wnt7a/b activity at the BBB might be dominated by site 1 of the NTD. Supporting this hypothesis, Reck binds Wnt7a/b exclusively

within the N-terminal domain (29, 31), and chimeric Wnt ligands composed of Wnt7a NTD fused to a CTD derived from another Wnt were competent for Reck binding, which correlated with Gpr124/Reck signaling (**fig. S4**).

This led to the exciting possibility that, in contrast to the systemic “off-target” situation where both contact sites 1 and 2 are strictly required for Wnt signaling (20, 34), Wnt7-Fz interaction at site 2 might become dispensable in the context of Gpr124/Reck-stimulated signaling. In line with this prediction, a hemisected Wnt7a variant, Wnt7a<sup>NTD</sup>, composed of the sole NTD domain, retained partial activity on Gpr124/Reck-mediated signaling while showing no stimulation of Fz5 signaling, used as a paradigm “off-target” readout (**Fig. 1B**). Furthermore, substituting three of the five Wnt7a residues involved in site 2 contacts into alanines did not affect Gpr124/Reck-mediated signaling, while reducing Fz5 signaling by more than 50% (**fig. S5**). Both the reciprocal single-domain CTD variant and Wnt7a<sup>S206A</sup> with impaired site 1 were fully inactive. Assuming comparable expression and secretion levels, site 1- and 2-inactive variants likely result from improper folding, inability to interact with Fz, or both. Together, these findings reveal that when presented by appropriate co-receptors, Wnt ligands can trigger Fz signaling even in the absence of the hydrophobic contacts of site 2. The signaling properties of Wnt7a<sup>NTD</sup> further demonstrated that altering the structure of Wnt ligands can modulate their signaling specificity, and more specifically, that Wnt7a can be engineered into a Gpr124/Reck-specific ligand.

Based on this proof of concept, we implemented a large-scale screen for Wnt7a variants with increased “on-target” activity, as Wnt7a<sup>NTD</sup> is only ~30% active compared to the parental Wnt7a ligand. To that end, we generated a collection of 147 single-residue variants of murine Wnt7a, in which surface-exposed charged or hydrophobic residues were mutated into alanine (or into arginine for alanine residues). This collection, the most comprehensive of any Wnt ligand,

corresponds to 46% of the residues of the secreted protein, and 51% of its exposed surface. Each variant was individually tested for its Gpr124/Reck-dependent and -independent activity (**Fig. 1C, D, fig. S6A, Table S2**). Wnt7a appeared highly sensitive to mutations when assessed on Fz5, with 37% of variants exhibiting <10% activity (red residues), and only 31% maintaining >70% activity (green residues). Unexpectedly, the large majority of critical residues are not located in the Fz binding sites. Hyperactive variants were also readily uncovered, with 5% of variants displaying over 2-fold higher Fz5 signaling activities than the natural ligand (*e.g.* K255A, K95A, K296A, K273A). This illustrates the evolution of Wnt ligand morphogens within carefully selected, submaximal activity windows. Although a systematic evaluation of ligand expression and secretion was not attempted, we assessed the secretion of all 17 variants inactive on both Fz5 and Gpr124/Reck. By virtue of their complete inactivity, these variants constitute preferential candidates for mis-trafficking or mis-expression and, therefore, probably overestimate the secretion failure rate. Yet, 88% (15/17) showed similar levels of extracellular accumulation as Wnt7a, ruling out improper trafficking as a leading cause for the large proportion of Fz5-inactive variants (**fig. S7**). Accordingly, the majority of Fz5-inactive and -overactive variants displayed unaltered Gpr124/Reck-dependent signaling. Indeed, in sharp contrast to Fz5, Gpr124/Reck signaling appeared homogenous and largely insensitive to Wnt7a variations, as 76% of the variants retained >70% activity (**Fig. 1C, D and fig. S6A**).

Notably, the enhanced Wnt7a signaling robustness associated with the presence of the BBB-specific co-receptors resulted in the identification of 25 single-residue variants displaying highly specific Gpr124/Reck activity (so-called “agonists” >70% on-target, <10% off-target), scattered over the entire Wnt7a structure (**Fig. 1D** residues highlighted in blue, **fig. S6B and Table S2**). Reciprocal Fz5-selective variants were not found. Among these single-residue Gpr124/Reck agonists, we selected the Wnt7a<sup>K190A</sup> variant as a prototype, optimally combining

a WT-like signal on Gpr124/Reck, and no “off-target” Fz5 activity (**Fig. 1C**, **fig. S6B** and **Table S2**).

*In vitro*, none of the transfected Fz receptors could be stimulated by Wnt7a<sup>NTD</sup> or Wnt7a<sup>K190A</sup> in the absence of Gpr124/Reck, an observation compatible with the strict selectivity of agonists (**Fig. 1E**). *In vivo*, in sharp contrast to Wnt7a, ubiquitous expression of Wnt7a<sup>NTD</sup> or Wnt7a<sup>K190A</sup> after mRNA injections failed to trigger ectopic Wnt activation during *Xenopus* (**Fig. 1F**), or zebrafish (**Fig. 1G**) gastrulation, as assessed by the absence of posteriorizing or gross morphological alterations. Although the expression level and secretion rate of Wnt7a<sup>NTD</sup> or Wnt7a<sup>K190A</sup> were not formally compared to Wnt7a *in vivo*, the agonists displayed “on-target” biological activities in zebrafish, implying that the lack of morphological defects is not a trivial consequence from a complete lack of activity (see below). Dose-response analyses following mRNA injections in the zebrafish zygote revealed that 3 pg of Wnt7a mRNA was sufficient to trigger “off-target” signaling, while Wnt7a<sup>NTD</sup> and Wnt7a<sup>K190A</sup> were remarkably well tolerated even when expressed in a 100-fold excess (**Fig. 1G**). Of note, Wnt7a signaling in this setting is Gpr124-independent, as revealed by the analysis of zygotic and maternal-zygotic *gpr124*<sup>s984</sup> mutants (27) (**fig. S1C**).

The morphological alterations induced, selectively, by Wnt7a mRNA injections may result either from a mere quantitative increase in Wnt signaling, as detected in cell culture using universal TOP-flash reporters, or from a qualitative difference between Gpr124/Reck-dependent and -independent signaling. To resolve this, we artificially expanded the expression domain of Gpr124/Reck by mRNA injections in zebrafish embryos. Under these conditions, both Wnt7a or Wnt7a<sup>K190A</sup> mRNA injections triggered morphological alterations at low doses (**fig. S8**). The developmental innocuity of Wnt7a<sup>K190A</sup> thus seemingly results predominantly, although we cannot say exclusively, from the restricted expression pattern of Gpr124/Reck.

Mechanistically, the selectivity of the uncovered agonists results from their incapacity to bind, and therefore activate, Fz receptors in the absence of Gpr124/Reck. Indeed, while Wnt7a immunolocalized to the surface of *RECK*<sup>-/-</sup>; *GPR124*<sup>-/-</sup> cells transiently transfected with Reck or Fz5, Wnt7a<sup>NTD</sup> and Wnt7a<sup>K190A</sup> labeled the membrane in the presence of Reck, but not Fz5 (**Fig. 2A, B**). Accordingly, the agonists bound HA-tagged Reck as efficiently as Wnt7a in anti-HA co-immunoprecipitation experiments (**Fig. 2C**) but lost the capacity to bind HA-Fz5 in *RECK*<sup>-/-</sup> cells (**Fig. 2D**). However, Fz5 binding was restored upon co-expression of Reck (**Fig. 2D**). These results imply either (i) that Reck binding influences the inherent structural modalities of Wnt/Fz interaction, as exemplified by the activity of the single-domain Wnt7a<sup>NTD</sup> lacking an essential contact site for autonomous Wnt/Fz signaling, or (ii) that Reck is required to keep Wnt7a ligands in an active configuration. Wnt ligands are indeed short-lived and rapidly lose activity by oligomerization, in a process that increases their hydrosolubility (35, 36). Reck has been shown to extend Wnt7a activity half-life by maintaining it in a monomeric, hydrophobic state (30, 37). The widespread distribution of the 25 Gpr124/Reck agonistic mutations over Wnt7a structure, their exposed position and the nature of introduced mutations make it unlikely that the mutations intrinsically affect the interaction chemistry with Fz.

It is thus possible that the introduction of single-residue variations into Wnt7a reduces ligand stability below a threshold required for Fz signaling, a property that the stabilizing action of Reck could counteract. In agreement, when assessed across the 147 Wnt7a variants, a clear correlation was seen at the single-residue level between Fz5 and Gpr124/Reck/Fz1 activities. Variants displaying even slightly reduced activity on Gpr124/Reck (yellow, orange, or red residues in **Fig. 1C, D**) were generally fully inactive in the more sensitive Fz5 setting (**Fig. 2E**). Conversely, preservation of at least partial Fz5 activity (orange, yellow, or green residues in **Fig. 1C, D**) strongly correlated with full activity on Gpr124/Reck (**Fig. 2E**). In summary, the

collection of variants seems to give a similar structure-function picture in both Wnt7a receptor settings, albeit at a dramatically different level of expressivity.

As stability of morphogens influences their range of action, with more stable ligands capable of activating more distant cells, we analyzed the capacity of Wnt7a and Wnt7a<sup>K190A</sup> to activate Wnt signaling at short distances (autocrine mono-cultures) versus longer distances (paracrine co-cultures) (**Fig. 2F**). While Wnt7a retained partial paracrine activity, Wnt7a<sup>K190A</sup> could not reach the receiving cell in an active form. Of note, the whole collection of agonists behaved similarly in this assay (**fig. S9**).

Together these results indicate that achieving Gpr124/Reck selective agonism relies not only on the ligand's intrinsic properties, but also on the spatial distribution of Wnt7a/b-releasing cells and Gpr124/Reck-positive receiving cells. Consequently, the structural window for agonist engineering is probably narrow, with even subtle mutations at risk of being detrimental for selectivity. In agreement, combining agonistic mutations invariably resulted in fully inactive ligands, even when tested on Gpr124/Reck signaling in mono-cultures (**Fig. 2G**). Conversely, introducing K95A, K255A, K273A, and K296A mutations into Wnt7a<sup>K190A</sup> (all of which increase Fz5 activity, **Fig. 1C**) was sufficient to abolish selectivity by restoring partial Fz5 signaling (**Fig. 2H**). Finally, mutating K190 to alternative residues (G, S, L, P, D, E, or R) had variable effects on signaling specificity. Mutations to small or hydrophobic residues (A, S, or L) conferred selectivity towards Gpr124/Reck. In contrast, mutations to helix breakers (G or P) or residues of opposed charges (D or E) abrogated activity, and the charge-preserving K to R substitution reduced Fz5 activity by over 50% (**Fig. 2I**). In sum, by recruiting Wnt7a/b into a higher-order receptor complex, Gpr124/Reck extends Wnt7a/b signaling robustness.

To test the functionality of the agonists *in vivo*, we generated a Wnt7a-deficiency model in zebrafish. Although the Gpr124/Reck complex was first discovered in zebrafish by its essential

role in cerebrovascular and dorsal root ganglia development (27), the exact nature of the Wnt7a/b ligand isoform implicated in these processes has not been explored. During mouse embryogenesis, Wnt7a and Wnt7b cooperate to control brain angiogenesis and BBB formation (11, 12). *Wnt7a* and *Wnt7b* are duplicated in the zebrafish genome (*wnt7aa*, *wnt7ab*, *wnt7ba*, and *wnt7bb*), and we used morpholino-mediated gene knock-down to identify the BBB-relevant ligand(s). Only *wnt7aa* morphants showed the anticipated phenotypes (**fig. S10A**) and, therefore, we generated a *wnt7aa* frame-shift allele (*wnt7aa<sup>ulb2</sup>*) through CRISPR/Cas9 mutagenesis (**Fig. 3A**). Homozygous *wnt7aa<sup>ulb2</sup>* mutants (*wnt7aa<sup>-/-</sup>*) displayed fully penetrant cerebrovascular defects in the 60 hours post fertilization (hpf) hindbrain (**Fig. 3B**), associated with down-regulated *Tg(7xTCF-Xla.Siam:GFP)* Wnt/ $\beta$ -catenin reporter expression in CNS-invading vessels (**Fig. 3C**). The development of *ngn1:GFP*-positive DRG neurons was also compromised (**Fig. 3B**), consistent with *wnt7aa* expression in the zebrafish brain and trunk region (**fig. S10B**). In cell cultures, all tested human, mouse, and zebrafish orthologues of the Wnt7/Gpr124/Reck signaling module were functionally interchangeable (**fig. S11**), authorizing the functional assessment of murine ligands in zebrafish.

The Gpr124/Reck-dependent DRG neurogenesis defects resulting from *wnt7aa* deficiency could be partially corrected by injecting 100 pg of Wnt7a<sup>NTD</sup> or Wnt7a<sup>K190A</sup> mRNA at the one-cell stage. In contrast, the parental Wnt7a could not restore DRG development as it triggered severe morphological defects (**Fig. 1G** and **3D**). These results not only demonstrate that these agonists can stimulate Gpr124/Reck activity *in vivo*, but also that they outperform Wnt7a by the lack of off-target effects (**Fig. 3D**). However, *Wnt7aa<sup>-/-</sup>* cerebrovascular phenotypes could not be rescued by transient mRNA expression, presumably due to the late onset of angiogenic sprouting in zebrafish hindbrain (36 hpf). Therefore, to test if Wnt7a<sup>NTD</sup> and Wnt7a<sup>K190A</sup> can also function as *bona fide* BBB instructive ligands, we assessed their activity by mosaic transgenic endothelial expression, using a *kdrl* (*vegfr2*) promoter. In this approach, Wnt7a<sup>K190A</sup>



restored the formation of central arteries (CtAs) in *wnt7aa*<sup>-/-</sup> embryos to a level comparable to Wnt7a, and these vessels expressed the glucose transporter-1 (Glut1), a marker of BBB maturation (**Fig. 3E**). Consistent with its partial activity *in vitro*, Wnt7a<sup>NTD</sup> was also competent for Gpr124/Reck-dependent brain angiogenesis and barrierogenesis, although less potently than Wnt7a<sup>K190A</sup>. This difference is compatible with a more limited intrinsic signaling potential (**Fig. 1E**), but we cannot exclude reduced protein expression or processing *in vivo*.

These results, demonstrating the capacity of the agonists (in particular Wnt7a<sup>K190A</sup>) to stimulate Wnt signaling at the BBB, led us to test their protective potential in disease models. In zebrafish larvae, pharmacological exposure to atorvastatin (ATV) is used as a non-invasive hemorrhagic stroke model, reminiscent of human cerebral cavernous malformation (CCM)-like lesions (38). While over 90% of ATV-exposed WT larvae displayed moderate to severe intracranial hemorrhages, transgenic endothelial expression of Wnt7a<sup>K190A</sup> profoundly decreased the extent of cerebrovascular ruptures, with over half of the injected embryos showing no or little intracerebral bleeding (**Fig. 3F**). ATV treatment also resulted in the accumulation of intracardially injected 10 kDa Dextran into the hindbrain (**Fig. 3G**). To test whether Wnt7a<sup>K190A</sup> expression could counteract these more subtle ATV-induced BBB defects, we examined Dextran-injected embryos with hemispheric transgenic endothelial expression of Wnt7a<sup>K190A</sup>, allowing to contrast CNS leakage among the two hemispheres of a single animal. Wnt7a<sup>K190A</sup> expression was sufficient to reduce the leakage to control levels (**Fig. 3H**).

Altogether, these results in zebrafish demonstrate the efficacy of the uncovered Gpr124/Reck agonists *in vivo* and led us to test their potential as BBB-protective agents in mammals. In order to deliver the agonists to the mouse CNS, we used the engineered AAV-PHP.eB capsids of adeno-associated viruses, reported to transduce over 55% of cortical and striatal neurons, as well as astrocytes and endothelial cells after a single peripheral intravenous injection (39). We

generated AAV-PHP.eB viruses expressing either EGFP alone (AAV-EGFP), Wnt7a-P2A-EGFP (AAV-Wnt7a), or Wnt7a<sup>K190A</sup>-P2A-EGFP (AAV-K190A) under the control of the constitutive CAG promoter. We validated that the Wnt7a fusions to EGFP via the cleavable P2A are active *in vitro*, and that upon intravenous injection of  $4 \cdot 10^{11}$  vg (viral genomes) in 8-week old mice, CD31-positive brain vessels are surrounded by EGFP<sup>+</sup> cells (**Fig. 4A**), exposing endothelial cells to local sources of Wnt7a or Wnt7a<sup>K190A</sup>. We confirmed that the AAV-PHP.eB capsid drives expression of the transgenes in ~25% of cortical and striatal ECs, in ~30% of astrocytes, and in ~45% of NeuN<sup>+</sup> neurons (**fig. S12A**). Over 95% of the examined Desmin<sup>+</sup> pericytes were negative for EGFP. EGFP<sup>+</sup>/Desmin<sup>+</sup> double positive cells were seemingly detected at rare occasions, although we could not exclude endothelial contributions. Pericytes are thus, at best, marginal sources of Wnt7a in this approach (**fig. S12B**).

Notably, although expressed from uniformly distributed cells, Wnt7a and Wnt7a<sup>K190A</sup> showed a discrete distribution, with preferential accumulation at the level of CD31-positive brain vessels, as well as some scattered parenchymal cells (**Fig. 4B**, asterisks). The distribution, and hence potential activity of the ligands, likely reflects the expression patterns of their receptors, with unbound ligands presumably getting cleared through the glymphatic system (40). Accordingly, Wnt7a, with its broader receptor repertoire, appeared to exhibit a more significant non-vascular distribution (**Fig. 4B**, asterisks). More so, immunodetection of  $\beta$ -catenin activity (LacZ signal) in coronal brain sections of BAT-GAL mice (41) revealed that, in contrast to Wnt7a<sup>K190A</sup>, Wnt7a triggered ectopic Wnt/ $\beta$ -catenin signaling in non-endothelial cells of the hippocampus and the parafascicular nucleus of the thalamus at all examined timepoints (7, 14, and 28 dpi) (**Fig. 4C**). These two areas are associated with high Fz5 expression (42, 43). Other brain regions did not exhibit increased LacZ signal, probably reflecting the restricted expression of Fz5 and Fz8 in the adult CNS (**fig. S13**). Wnt transgenic reporter systems, like BAT-GAL mice, using an artificial reporter construct with concatemered TCF/LEF sites, do not always

reliably report *in vivo* Wnt activities due to random variegation in transgene expression (28, 44). To verify the Wnt activity patterns revealed by the BAT-GAL model, we performed RNAScope hybridization of *Axin2* mRNA, possibly the transcript most reliably correlated with Wnt activity across tissues (45–47). This approach confirmed the ectopic activation of Wnt signaling induced by Wnt7a, but not Wnt7a<sup>K190A</sup>, at both 14 dpi (**Fig. 4D**) and 32 dpi (**fig. S14**) in the hippocampus and the parafascicular nucleus of the thalamus. While the ectopic Wnt7a activities did not result in obvious behavioral defects in adult mice (**fig. S15**), gene delivery of Wnt7a, but not Wnt7a<sup>K190A</sup>, was detrimental to neonatal mouse development as revealed by impaired spontaneous locomotor activity (**Fig. 4E**). We next focused on the Wnt activity status at the target BBB endothelium. Endothelial Wnt activity is low in adult mice (48) and could only rarely be detected in BAT-GAL reporter mice, irrespective of Wnt7a or Wnt7a<sup>K190A</sup> expression (**fig. S13**). Therefore, we stained for Lymphoid Enhancer Binding Factor 1 (LEF1), a key mediator of Wnt/ $\beta$ -catenin signaling, which robustly labeled ~80% endothelial cells throughout the different brain regions. AAV-based delivery of Wnt7a or Wnt7a<sup>K190A</sup> did not increase LEF1 signals in ECs (**fig. S16**).

The absence of “off-target” Wnt signaling activity after widespread gene delivery of Wnt7a<sup>K190A</sup> in the mouse brain prompted us to test the therapeutic potential of the Gpr124/Reck agonist in CNS pathologies associated with BBB dysfunction, starting with grade IV astrocytoma or glioblastoma multiforme (GBM). GBM, the most aggressive and frequent primary brain tumor, is characterized by a dense vascular network exhibiting disrupted BBB properties (49). Interestingly, endothelial Wnt signaling was reported to control vascular integrity in different brain tumor models (16, 50, 18, 51). This led us to evaluate the impact of Gpr124/Reck-specific activators on GBM tumor growth, vascularization, and BBB integrity. Two days after orthotopic implantation of  $1.10^5$  GL261 tumor cells into the C57BL/6 mouse striatum, we performed a single “hit-and-run” intravenous AAV-PHP.eB gene delivery and

monitored tumor volume by MRI at 21-24 days post-implantation (dpi) (**Fig. 5A**). While control tumor expansion was highly variable, with volumes ranging from 10 to 80 mm<sup>3</sup>, Wnt7a<sup>K190A</sup> expression (AAV-K190A) reduced this variability and restricted tumor volume to an average value of 20 mm<sup>3</sup>. In particular, the proportion of larger tumors (> 40 mm<sup>3</sup>) was reduced upon Wnt7a<sup>K190A</sup> gene delivery (8% in K190A cohorts versus 33% in controls).

At 25 dpi, mice with the largest tumors started to exhibit disease symptoms, including faulty postural syndromes and abnormal gait. This timepoint was therefore chosen for terminal analysis and tissue harvesting. Control tumors showed more prominent intratumoral microvascular hemorrhages (asterisks) and edema than AAV-K190A tumors (**Fig. 5B**), suggesting cerebrovascular differences between the groups. Accordingly, the tumor-associated vasculature showed features of vessel normalization, *i.e.* reduced CD31<sup>+</sup> vascular density (**Fig. 5C**), reduced vessel diameter (**Fig. 5C**), and more compact and seemingly smoother distribution of laminin (**Fig. 5D**). Cell densities were comparable in AAV-EGFP and AAV-K190A tumors (6,425 versus 7,141 cells.mm<sup>-2</sup>, respectively). This implies that the total number of cells is smaller in AAV-K190A tumors, most likely as a consequence of reduced tumor cell proliferation. The modest differential cellular densities reflect, however, a contribution of vasogenic edema to the larger volumes of AAV-EGFP tumors. Assessment of  $\beta$ -catenin transcriptional response by immunodetection of nuclear LEF-1 confirmed previous reports of reduced endothelial Wnt signaling in GBM vessels (**Fig. 5E**) (18). Wnt7a<sup>K190A</sup> successfully restored Wnt activity in the tumor endothelium, reaching a level remarkably similar to the steady-state activity of non-tumoral parenchymal vessels. In contrast, it did not significantly affect LEF1 levels in vessels of the contralateral hemisphere (**Fig. 5E**), confirming the findings in healthy mice (**fig. S16**). We postulate that homeostatic feedback regulations poise endothelial Wnt activity levels at a physiological setpoint value, insensitive to ectopic external stimuli. This observation could explain the lack of detectable phenotypes in AAV-K190A mice, with Wnt

activity increased selectively at the dysfunctional BBB, leaving the healthy brain unaltered. In agreement with LEF-1 nuclear accumulation, we observed re-establishment of BBB integrity in tumor vessels, as assessed by increased GLUT1 immunostaining (**Fig. 5F**) and reduced endogenous fibrinogen extravasation (**Fig. 5G**). Interestingly, the restoration of GLUT1 signal in the tumor vasculature of AAV-K190A mice was linked to reduced tumor parenchymal GLUT1 signal, paralleling the developmental switch of GLUT1 expression from the neuroepithelium to the vessels upon CNS vascularization (11, 12).

To determine the source of Wnt7a<sup>K190A</sup> within the tumor microenvironment, we analyzed the distribution of the EGFP transduction marker on coronal tumor sections. Glioblastoma cells were negative, as expected from the non-replicate nature of AAV genomes, and the numerous cell divisions of these cells upon implantation (**fig. S17**). Within the tumor, 30% of CD31<sup>+</sup> endothelium was EGFP<sup>+</sup>, and blood vessels accounted for ~60% of the total intratumoral EGFP<sup>+</sup> signal (**fig. S17**). In addition, the EGFP signals were particularly intense in S100 $\beta$ <sup>+</sup>/GFAP<sup>-</sup> astrocytes of the tumor glial scar. Iba1<sup>+</sup> microglial cells were EGFP<sup>-</sup> (**fig. S17**). Together, if we assume that EGFP is a reliable indicator for Wnt7a expression, the seemingly most prominent sources for Wnt7a<sup>K190</sup> are the ECs themselves and the peritumoral reactive astrocytes.

Combined with the intrinsic variability associated with *in vivo* delivery of AAV particles, these relatively discrete Wnt7a<sup>K190A</sup> sources resulted in surprisingly uniform effects on tumor growth (**Fig. 5A**). Even more so, in view of the considerable heterogeneity associated with control tumors (**Fig. 5A**). Given that (i) GBM tumor vessels derive by vessel co-option or angiogenesis from pre-existing Wnt-positive parenchymal vessels, (ii) endothelial Wnt activity levels drop in the GL261 vasculature, and (iii) endothelial Wnt signaling slows down GL261 tumor progression, we reasoned that the heterogeneity of GL261 tumor growth could result from

varying degrees of residual endothelial Wnt signaling levels. Supporting this hypothesis, endothelial LEF1 and GLUT1 levels were somewhat heterogeneous in control tumors (**Fig. 5E, F**). Strikingly, both markers are inversely correlated with vessel density, fibrinogen leakage, and tumor volume (**Fig. 5H**). These correlations suggest that the growth rate of GL261 tumors is at least partially determined by the level of residual Wnt signaling of its perfusing vasculature, and that AAV-delivery of Wnt7a<sup>k190A</sup> is sufficient to uniformly raise the signaling level to promote neurovascular normalization and tumor growth reduction (**Fig. 5I**).

The variable degree of residual endothelial Wnt signaling within the WT GL261 tumor endothelium complicated the analysis of the mechanism underlying endothelial Wnt-induced BBB repair. Therefore, we resorted to transgenic Tet-Off GL261 cells that conditionally express the secreted Wnt inhibitor Dkk1 (dickkopf WNT signaling pathway inhibitor 1) (*16*). When exposed to doxycycline, these cells potently repress Dkk1 expression *in vitro* and *in vivo*, without affecting their intrinsic *in vitro* growth rate (**fig. S18**). Upon implantation, the characteristics of Dkk1<sup>+</sup> (-dox) GL261 tumors (Wnt inhibition) were compared with Dkk1<sup>-</sup> (+dox) tumors of mice injected with AAV-EGFP (control) or AAV-K190A (Wnt activation). As expected, Dkk1<sup>-</sup> tumors grew and responded to AAV-K190A as WT GL261 cells, with 95% of the AAV-K190A-treated tumors smaller than 40 mm<sup>3</sup> at 20-24 dpi and the control cohort exhibiting more variable volumes (40-80 mm<sup>3</sup>) (**Fig. 6A**). Dkk1<sup>+</sup> tumors grew even bigger, up to 160 mm<sup>3</sup> (**Fig 6A**). Endothelial Wnt activity markers (LEF1 and GLUT1) were the highest in the Wnt stimulated Dkk1<sup>-</sup>/K190A tumors and the lowest in Wnt inhibitory Dkk1<sup>+</sup> tumors, with Dkk1<sup>-</sup>/EGFP tumors showing intermediate values (**fig. S19A,B**). As anticipated, hemorrhage (**fig. S20**), vascular density (**fig. S19C**), and fibrinogen leakage (**Fig. 6B**) followed the opposite trend, being gradually reduced by the step-wise increase in endothelial Wnt signaling.

The restoration of BBB impermeability to fibrinogen (350 kDa) demonstrates that  $Wnt7a^{K190A}$  can prevent BBB permeability to large molecules. In contrast, small molecule 557 Da sulfo-NHS-Biotin leaked within the tumor parenchyma of all examined tumors, irrespective of their endothelial Wnt activation level. Of note however,  $Dkk1^+$  tumors exhibited slightly higher leakage values (**Fig. 6C**). To define the mechanism of K190A-induced BBB repair to protein-sized tracers, we examined tumor and cortical vessels by electron-microscopy following intravenous injection of 44 kDa horseradish peroxidase (HRP) (**Fig. 6D**). In the healthy mouse cerebral cortices, blood-borne peroxidase was detected by the electron-dense 3-3' diaminobenzidine (DAB) reaction product that only penetrated the intercellular spaces of adjacent endothelial cells over small distances. The signal sharply stopped at presumptive tight junctions (arrowheads), as typically reported in healthy BBB vessels (52). As expected, the electron density of the endothelial basement membranes (black asterisks) was consequently much lower as compared to the lumen (white asterisks), consistent with luminal HRP retention. This spatially restricted distribution of HRP contrasted sharply with the signal observed along the entire length of the intercellular spaces of  $Dkk1^+$  and  $Dkk1^-/EGFP$  tumor vessels. In these dysfunctional vessels, no difference was found between HRP levels within blood vessel lumens and their basement membranes. However, mice injected with AAV-K190A exhibited tumor vessels that reverted to a WT phenotype, with a clear boundary at the level of the tight junction kissing points (arrowheads, **Fig. 6D**). These findings are compatible with the hypothesis that AAV-K190A partially corrects the tight-junctional defects of glioblastoma vessels. On a cautionary note, we cannot formally exclude that the accumulation of HRP within the basement membranes and basolateral side of the interendothelial clefts results, at least in part, from HRP leaks associated with more distant hemorrhages. However, in line with the electron micrographs, Claudin-5 immunostaining appeared denser in AAV-K190A tumor vessels, compatible with a direct role of  $Wnt7a^{K190A}$  on endothelial tight junctions (**Fig. 6E**).

The significant intra-tumoral leak of HRP resulted in modest electron-dense contrast, making unambiguous scoring of transcytosis vesicles in glioblastoma vessels impractical. Mfsd2a, an endothelium-specific inhibitor of caveolae-mediated transcytosis (52), was, however, increased by endothelial Wnt activation (**Fig. 6F**), as previously reported at the blood-retinal barrier (53). Accordingly, Caveolin-1 levels were lowered by AAV-K190A (**fig. S21**). The pericytes loss, typically associated with glioblastoma (16, 18) and upregulated transcytosis (52), could also be partially counteracted by AAV-K190A (**Fig. 6G**). Altogether, in GL261 tumors, Wnt7a<sup>K190A</sup> restores endothelial Wnt signaling, reduces vascular density and normalizes the BBB pleiotropically, affecting both the transcellular and paracellular permeability routes, thereby slowing tumor progression.

As proof-of-concept that the BBB protective properties of the uncovered Gpr124/Reck agonists could have implications in CNS disorders of radically different etiology and BBB dysfunction kinetics, we turned to large-vessel and focal transient ischemic stroke models in mice. After stroke, surgical or pharmacological recanalization therapies are crucial to promptly restore perfusion of the ischemic penumbra, a rim of cells whose survival will depend on the timing of recanalization. However, upon salutary blood flow restoration, reperfusion-associated tissue injury leads to BBB damage and contributes to worsening outcomes (1, 54). To establish whether Gpr124/Reck-stimulated Wnt signaling at the BBB could mitigate the infarct size by limiting post-stroke injury, AAV-EGFP and AAV-K190A injected mice were subjected to transient middle cerebral artery occlusions (tMCAO). 2,3,5-Triphenyltetrazolium chloride (TTC) staining of whole-brain coronal sections revealed a significantly reduced infarct volume upon Wnt7a<sup>K190A</sup> expression (**Fig. 6H**). This reduction is consistent with previously reported effects of conditional endothelial  $\beta$ -catenin stabilization (18). A similar beneficial effect was observed in a transient focal endothelin-1 (ET-1) stroke model (**Fig. 6I**), but not in a permanent,



photo-thrombotic (PT) stroke model (**Fig. 6I**) tentatively assigning the protective effects of Wnt7a<sup>K190A</sup> to the post-stroke reperfusion process.

## Discussion

Altogether, we discovered that Wnt7a ligands can be engineered into highly-specific Gpr124/Reck agonists, thereby disclosing a novel class of BBB therapeutics. This level of specificity was deemed unreachable for Wnt-derived proteins by virtue of their promiscuous interaction mode with widely expressed Fz receptors.

In contrast to Wnt7a, the uncovered Gpr124/Reck agonists were remarkably well tolerated *in vivo* despite the broad expression strategies adopted in this study. In *Xenopus* and zebrafish, their ubiquitous expression during the Wnt-sensitive steps of cleavage, gastrulation, somitogenesis, and early organogenesis failed to yield detectable morphological alterations, even when expressed in a 100-fold excess to the highest developmentally tolerated dose of the parental Wnt7a. In mice, CNS-wide expression of Gpr124/Reck agonists via AAV-PHP.eB gene delivery did not trigger ectopic Wnt activation. Accordingly, injected mice did not show any detectable adverse phenotype, even after several months. In addition to the strict signaling specificity of the Gpr124/Reck agonists, we suspect that homeostatic feedback loops maintain Wnt signaling activities within carefully controlled physiological activity windows. Accordingly, we detected significant reinforcement of endothelial Wnt signaling only in dysfunctional glioma vessels, while the signaling levels of healthy parenchyma vessels remained unaffected.

We believe that the Gpr124/Reck agonists described in this study constitute promising BBB therapeutic molecules. However, their inactivity in other Wnt7a/b signaling settings, most notably non-canonical Wnt pathways, remains to be tested. In addition, a significant intrinsic limitation to their use lies in their lipophilicity, currently restricting their use to disease settings

where gene delivery could be envisaged. While this complicates interventions in acute conditions like stroke or traumatic brain injury, the uncovered Gpr124/Reck agonists might be well-positioned for more slowly progressing disorders like neurodegenerative disorders (Alzheimer's disease or ALS) or glioblastoma. In glioblastoma, intra-tumoral BBB leakage leads to morbid vasogenic brain edema. GBM is therefore well-positioned for targeted vascular therapies (55), and systemic administration of bevacizumab, an anti-VEGF antibody, is used as second-line treatment for recurrent or non-responsive glioblastomas. It would be interesting to compare or combine Gpr124/Reck agonists and anti-VEGF strategies in different glioblastoma molecular subtypes, and analyze their impact on tumor angiogenesis, vessel co-option, BBB, and chemotherapy (56, 57, 51). In complement, developing stable injectable biologicals activating Gpr124/Reck signaling, including structurally unrelated surrogates (58–61), seems a promising strategy for several brain disorders occurring on a more acute timescale. The therapeutic scope of Wnt therapies at the BBB through Gpr124/Reck agonism is difficult to predict. Intriguingly, for a signal transduction pathway leading to gene transcription regulation, the protective impact of Wnt cannot faithfully be inferred from the transcriptomic landscape of the diseased BBB endothelium. While glioblastoma endothelium displays an aberrant Wnt expression signature (18), the post-stroke endothelium does not (54, 62). Instead, multiple etiologically distinct disorders converge to a common disease BBB transcriptomic signature, reminiscent of peripheral endothelia (62). This observation suggests that mimicking the NVU niche microenvironment by reinstalling the priming Wnt7a signal, might have a broader impact than what can rationally be inferred from transcript profiling or biomarker analysis.

Alternative strategies are being pursued to restore BBB function in disease, most notably relying on protein C-mediated activation of endothelial PAR-1 signaling (63) or PDGF-C

inhibition within the NVU (64). Both approaches are being evaluated in clinical trials for several acute and progressive neuropathologies, underscoring the broad potential of BBB-centered therapeutic approaches. As a contrasting strategy to these approaches, we here repurposed a key developmental BBB-inductive signal, acting at the top of the differentiation cascade that primes endothelial cells for BBB development. Wnt/ $\beta$ -catenin signaling has potential for pleiotropic actions in BBB restoration. As also reflected in this study, it has been implicated in many aspects of BBB physiology. This includes expression of tight junction proteins and solute transporters, suppression of vesicular transport, reduction of plasmalemma vesicle-associated protein (PLVAP) expression, and pericyte recruitment via control of PDGF-B secretion levels (10–12, 16, 13–15).

The neurovascular phenotypes reversed by the reinstatement of Wnt7a in disease conditions underscore the enduring plasticity of the BBB phenotype up to adulthood (13). They also demonstrate that the molecular signaling machinery set in place during early embryogenesis prevails in adults, ready to be activated for reinitialization of the BBB differentiation cascade. Finally, our findings exemplify that the BBB-inductive Wnt7a signals can partially override the deleterious effects of the BBB-disruptive agents typically associated with glioblastoma or stroke, most notably angiogenic growth and permeability factors like VEGF, pro-inflammatory cytokines and reactive oxygen species.

In summary, we have defined a novel modality to treat CNS disorders by healing the BBB. BBB-focused intervention strategies have unique potential as disease-modifying treatments in a variety of neuropathologies in addition to the conditions explored in this study, including multiple sclerosis, epilepsy and neurodegenerative disorders like Alzheimer's disease.

## **Acknowledgments:**

We thank C. Hénin, G. Oldenhove, S. Rosar, E. Dupont, L. Conrard, E. Zindy, V. Micha, N. De Henau, F. Andris, M.I. Garcia (ULB), K. Somme (GUF), M.S. Jeffers and G.O. Cron (Ottawa Hospital) and J.C. Paterna (Neuroscience Center Zurich) for their help. We thank D.L. Silver for the anti-Mfsd2a antibodies. We are grateful to P. Gut (Nestlé Institute of Health Sciences), O.A. Stone (Oxford, UK) and D.Y.R. Stainier (MPI, Germany) for helpful comments on the manuscript. **Funding:** M.E. and N.B. are FRIA fellows from the FRS–FNRS. S.V. and P.C. are postdoctoral researchers of the FRS–FNRS. Work in the B.V. laboratory is supported by FNRS (MIS F.4543.15), the Concerted Research Action (ARC), the Fondation ULB, the European Union HORIZON 2020 ITN "BtRAIN", the Queen Elisabeth Medical Foundation (Q.E.M.F.), the FRFS-WELBIO (CR-2017S-05R) and the ERC (GoG Ctrl-BBB 865176). S.L. was supported by the Deutsche Forschungsgemeinschaft (DFG) via the research group FOR2325 "The Neurovascular Interface" (LI 911/5-1), the individual project LI 911/7-1, as well as via the Excellence Cluster Cardio-Pulmonary Institute (CPI), the European Union HORIZON 2020 ITN "BtRAIN", the German Centre for Heart and Circulation Research (DZHK, Column B: Shared Expertise) and by the LOEWE CePTER Epilepsy Research Center of the state Hesse. AKE is Research Director of FRS–FNRS, supported by FRS–FNRS and the Fondation Simone et Pierre Clerdent. B.L. is supported by the Heart and Stroke Foundation of Canada, grant #G-17-0018290, the Canadian Institute of Health Research, grant # 388805, and by the New Frontiers Research Funds–Exploration, grant # NFRFE-2019-00641. The CMMI is supported by the European Regional Development Fund and the Walloon Region. **Author contributions:** All authors performed research and/or analyzed data. All authors discussed results and edited the manuscript. M.M. and B.V. wrote the manuscript. B.V. supervised the study. **Competing interests:** The ULB has filed a patent on the neurological applications of the Gpr124/Reck-mediated signaling mechanism. B.V. is a founder, stockholder and consultant of NeuVasQ

Biotechnologies. **Data and materials availability:** All data are available in the main text or the supplementary materials. Correspondence and requests for materials should be addressed to B.V.

## **Supplementary Materials**

Material and Methods

Figs. S1 to S21

Table S1 to S2

## References

1. B. Obermeier, R. Daneman, R. M. Ransohoff, *Nat. Med.* **19**, 1584–1596 (2013).
2. B. W. Chow, C. Gu, *Trends Neurosci.* **38**, 598–608 (2015).
3. M. Blanchette, R. Daneman, *Mech. Dev.* **138**, 8–16 (2015).
4. Z. Zhao, A. R. Nelson, C. Betsholtz, B. V. Zlokovic, *Cell.* **163**, 1064–1078 (2015).
5. C. P. Profaci, R. N. Munji, R. S. Pulido, R. Daneman, *J. Exp. Med.* **217** (2020), doi:10.1084/jem.20190062.
6. U. Lendahl, P. Nilsson, C. Betsholtz, *EMBO Rep.* **20**, e48070 (2019).
7. M. K. Montgomery *et al.*, *Cell Rep.* **31**, 107500 (2020).
8. A. Montagne *et al.*, *Nature*, 1–6 (2020).
9. M. D. Sweeney, Z. Zhao, A. Montagne, A. R. Nelson, B. V. Zlokovic, *Physiol. Rev.* **99**, 21–78 (2019).
10. S. Liebner *et al.*, *J. Cell Biol.* **183**, 409–417 (2008).
11. J. M. Stenman *et al.*, *Science.* **322**, 1247–1250 (2008).
12. R. Daneman *et al.*, *Proc. Natl. Acad. Sci. U. S. A.* **106**, 641–646 (2009).
13. Y. Wang *et al.*, *Cell.* **151**, 1332–1344 (2012).
14. Y. Zhou *et al.*, *J. Clin. Invest.* **124**, 3825–3846 (2014).
15. M. Hupe *et al.*, *Sci. Signal.* **10** (2017), doi:10.1126/scisignal.aag2476.
16. M. Reis *et al.*, *J. Exp. Med.* **209**, 1611–1627 (2012).
17. J. E. Lengfeld *et al.*, *Proc. Natl. Acad. Sci.* **114**, E1168–E1177 (2017).
18. J. Chang *et al.*, *Nat. Med.* **23**, 450–460 (2017).
19. R. Nusse, H. Clevers, *Cell.* **169**, 985–999 (2017).
20. C. Y. Janda, D. Waghray, A. M. Levin, C. Thomas, K. C. Garcia, *Science.* **337**, 59–64 (2012).
21. B. A. Parr, A. P. McMahon, *Nature.* **374**, 350–353 (1995).
22. A. C. Hall, F. R. Lucas, P. C. Salinas, *Cell.* **100**, 525–535 (2000).
23. M. Moreno-Estellés *et al.*, *Stem Cells Dayt. Ohio.* **30**, 2796–2809 (2012).
24. C. F. Bentzinger *et al.*, *Cell Stem Cell.* **12**, 75–87 (2013).

25. S. Yoshioka *et al.*, *Mol. Cancer Res. MCR.* **10**, 469–482 (2012).
26. Y. Wang *et al.*, *Tumour Biol. J. Int. Soc. Oncodevelopmental Biol. Med.* **36**, 8781–8787 (2015).
27. B. Vanhollebeke *et al.*, *eLife.* **4** (2015), doi:10.7554/eLife.06489.
28. C. Cho, P. M. Smallwood, J. Nathans, *Neuron.* **95**, 1056-1073.e5 (2017).
29. M. Eubelen *et al.*, *Science.* **361** (2018), doi:10.1126/science.aat1178.
30. M. Vallon *et al.*, *Cell Rep.* **25**, 339-349.e9 (2018).
31. C. Cho, Y. Wang, P. M. Smallwood, J. Williams, J. Nathans, *eLife.* **8** (2019), doi:10.7554/eLife.47300.
32. Y. Zhou, J. Nathans, *Dev. Cell.* **31**, 248–256 (2014).
33. E. Posokhova *et al.*, *Cell Rep.* **10**, 123–130 (2015).
34. S. Kumar *et al.*, *BMC Biol.* **12**, 44 (2014).
35. X. Zhang *et al.*, *Cell.* **149**, 1565–1577 (2012).
36. S. Kakugawa *et al.*, *Nature.* **519**, 187–192 (2015).
37. H. Li *et al.*, *iScience.* **19**, 559–571 (2019).
38. S. Eisa-Beygi, G. Hatch, S. Noble, M. Ekker, T. W. Moon, *Dev. Biol.* **373**, 258–266 (2013).
39. K. Y. Chan *et al.*, *Nat. Neurosci.* **20**, 1172–1179 (2017).
40. N. A. Jessen, A. S. F. Munk, I. Lundgaard, M. Nedergaard, *Neurochem. Res.* **40**, 2583–2599 (2015).
41. S. Maretto *et al.*, *Proc. Natl. Acad. Sci. U. S. A.* **100**, 3299–3304 (2003).
42. C. Liu, Y. Wang, P. M. Smallwood, J. Nathans, *J. Neurosci.* **28**, 5641–5653 (2008).
43. M. Sahores, A. Gibb, P. C. Salinas, *Dev. Camb. Engl.* **137**, 2215–2225 (2010).
44. A. A. A. van de Moosdijk, Y. B. C. van de Grift, S. M. A. de Man, A. L. Zeeman, R. van Amerongen, *Genes. N. Y. N 2000.* **58**, e23387 (2020).
45. B. Lustig *et al.*, *Mol. Cell. Biol.* **22**, 1184–1193 (2002).
46. E. Jho *et al.*, *Mol. Cell. Biol.* **22**, 1172–1183 (2002).
47. J. Y. Leung *et al.*, *J. Biol. Chem.* **277**, 21657–21665 (2002).
48. M. Corada *et al.*, *Circ. Res.* **124**, 511–525 (2019).

49. S. Watkins *et al.*, *Nat. Commun.* **5**, 1–15 (2014).
50. T. N. Phoenix *et al.*, *Cancer Cell.* **29**, 508–522 (2016).
51. A. Griveau *et al.*, *Cancer Cell.* **33**, 874–889.e7 (2018).
52. A. Ben-Zvi *et al.*, *Nature.* **509**, 507–511 (2014).
53. Z. Wang *et al.*, *Sci. Adv.* **6**, eaba7457 (2020).
54. R.-I. Kestner *et al.*, *Front. Neurosci.* **14**, 280 (2020).
55. P. Carmeliet, R. K. Jain, *Nat. Rev. Drug Discov.* **10**, 417–427 (2011).
56. T. Sandmann *et al.*, *J. Clin. Oncol. Off. J. Am. Soc. Clin. Oncol.* **33**, 2735–2744 (2015).
57. L. Erdem-Eraslan *et al.*, *Cancer Res.* **76**, 525–534 (2016).
58. C. Y. Janda *et al.*, *Nature.* **545**, 234–237 (2017).
59. Y. Tao *et al.*, *eLife.* **8**, e46134 (2019).
60. H. Chen *et al.*, *Cell Chem. Biol.* (2020), doi:10.1016/j.chembiol.2020.02.009.
61. R. Chidiac *et al.*, *EMBO Mol. Med.* **13**, e13977 (2021).
62. R. N. Munji *et al.*, *Nat. Neurosci.* **22**, 1892–1902 (2019).
63. J. H. Griffin, J. A. Fernández, P. D. Lyden, B. V. Zlokovic, *Thromb. Res.* **141 Suppl 2**, S62–64 (2016).
64. S. A. Lewandowski, L. Fredriksson, D. A. Lawrence, U. Eriksson, *Pharmacol. Ther.* **167**, 108–119 (2016).
65. J. H. Berger, M. J. Charron, D. L. Silver, *PloS One.* **7**, e50629 (2012).
66. F. A. Ran *et al.*, *Nature.* **520**, 186–191 (2015).
67. S.-W. Jin, D. Beis, T. Mitchell, J.-N. Chen, D. Y. R. Stainier, *Dev. Camb. Engl.* **132**, 5199–5209 (2005).
68. N. C. Chi *et al.*, *Genes Dev.* **22**, 734–739 (2008).
69. E. Moro *et al.*, *Dev. Biol.* **366**, 327–340 (2012).
70. H. F. McGraw, A. Nechiporuk, D. W. Raible, *J. Neurosci. Off. J. Soc. Neurosci.* **28**, 12558–12569 (2008).
71. D. Traver *et al.*, *Nat. Immunol.* **4**, 1238–1246 (2003).
72. L.-E. Jao, S. R. Wenthe, W. Chen, *Proc. Natl. Acad. Sci.* **110**, 13904–13909 (2013).
73. C. Thisse, B. Thisse, *Nat. Protoc.* **3**, 59–69 (2008).



74. C. B. Kimmel, W. W. Ballard, S. R. Kimmel, B. Ullmann, T. F. Schilling, *Dev. Dyn. Off. Publ. Am. Assoc. Anat.* **203**, 253–310 (1995).
75. A.-K. Kraeuter, P. C. Guest, Z. Sarnyai, *Methods Mol. Biol. Clifton NJ.* **1916**, 105–111 (2019).
76. M. Reis *et al.*, *J. Exp. Med.* **209**, 1611–1627 (2012).
77. S. Gurnik *et al.*, *Acta Neuropathol. (Berl.)*. **131**, 753–773 (2016).
78. L. Belayev *et al.*, *Stroke*. **34**, 758–763 (2003).
79. M. J. Shensa, *IEEE Trans. Signal Process.* **40**, 2464–2482 (1992).

## Figure legends

### Figure 1. Engineering Wnt7a ligands into highly specific Gpr124/Reck activators

(A) Backbone model of murine Wnt7a based on the crystal structure of CRD-bound XWnt8a (20), and schematics of the receptor complexes mediating Wnt7a/b/ $\beta$ -catenin signaling. (B) Models of Wnt7a, the Wnt7a<sup>S206A</sup> palmitoylation mutant, and the single-domain Wnt7a variants (N-terminal domain, NTD blue; C-terminal domain, CTD, grey) and their relative STF (super top flash) luciferase activity in the presence of Fz5 (grey) or Gpr124/Reck/Fz1 (green). (C) Position and color-coded Gpr124/Reck/Fz1 or Fz5 STF activities of 147 single-residue Wnt7a variants. Gpr124/Reck agonists (blue dots) were defined as variants with >70% Gpr124/Reck/Fz1 and <10% Fz5 activity. (D) Front, lateral, and back views of the Wnt7a surface model with integrated color-coded activities of all 147 single-residue variants. Agonistic mutations are highlighted in blue. (E) Beta-catenin signaling assays using STF cells transfected with any of the 10 Fz receptors or Gpr124/Reck, together with Wnt7a, Wnt7a<sup>NTD</sup>, Wnt7a<sup>K190A</sup>, or the empty pCS2 vector. (F) Phenotypic scoring of stage 36 *Xenopus laevis* embryos injected into the ventral vegetal region of the 4-cell embryo with 15 pg of the indicated mRNA. (G) Phenotypic scoring of 3 dpf zebrafish larvae injected at the one-cell stage with Wnt7a, Wnt7a<sup>NTD</sup>, or Wnt7a<sup>K190A</sup> mRNA at the indicated doses. \*\*\*P<0.001; data represent mean  $\pm$  SD.

## Figure 2. Gpr124/Reck agonists are unable to bind Fz autonomously

(A-B) *GPR124*<sup>-/-</sup>;*RECK*<sup>-/-</sup> HEK293 cells transiently expressing Wnt7a, Wnt7a<sup>NTD</sup>, or Wnt7a<sup>K190A</sup> together with Fz5, Reck, or the empty pCS2 vector were submitted to Wnt7a double immunostaining before (Wnt7a extracellular, green/black) and after (Wnt7a intracellular, pink) cell permeabilization. Maximum intensity projections of confocal images are shown (A), and the ratio between the membrane-associated and the intracellular signal (B) was calculated as described in the method section. (C-D) Western blot analysis of anti-HA co-immunoprecipitation assays after membrane-impermeable cross-linking in total lysates of *RECK*<sup>-/-</sup> HEK293T cells expressing HA-Reck (C) or HA-Fz5 (D) (bait) together with Wnt7a, Wnt7a<sup>NTD</sup>, or Wnt7a<sup>K190A</sup> (prey), with or without expression of untagged Reck (D). (E) Gpr124/Reck/Fz1 and Fz5 activity correlations across the Wnt7a single-residue collection. (F) Relative STF luciferase activity in the presence of Gpr124/Reck/Fz1 (green) or Fz5 (grey) in response to Wnt7a or Wnt7a<sup>K190A</sup> secreted either by the STF reporter cells (autocrine monoculture setting) or by co-cultured HEK293T cells (paracrine co-culture setting). (G, H, I) Gpr124/Reck/Fz1 (green) or Fz5 (grey) STF activities with combined agonistic mutations (G), activity-increasing mutations (H), or alternative substitutions of Wnt7a<sup>K190</sup> (I). \*\*\*P<0.001; ns: non-significant; data represent mean ± SD.

**Figure 3. Gpr124/Reck agonists stimulate brain angiogenesis, blood-brain barrier induction and prevent hemorrhagic stroke in zebrafish**

(A) Characterization of the zebrafish 7-bp frameshift *wnt7aa<sup>ulb2</sup>* allele. The protospacer adjacent motif (PAM) is underlined in blue. (B) Dorsal views and quantification of 60 hpf *Tg(kdrl:GFP)* hindbrain CtAs (central arteries) and 72 hpf *Tg(neurog1:GFP)* trunk dorsal root ganglia (DRG, grey arrowheads) in WT and *wnt7aa<sup>-/-</sup>* zebrafish. (C) Dorsal views of 30 hpf *Tg(7xTCF-Xia.Siam:GFP);Tg(kdrl:ras-mCherry)* hindbrains from WT and *wnt7aa<sup>-/-</sup>* embryos and quantification of the number of GFP+ ( $\beta$ -catenin signaling positive) endothelial cells in the perineural PHBCs (primordial hindbrain channels). (D) Trunk DRG development in 72 hpf *Tg(neurog1:GFP)* *wnt7aa* morphant larvae injected at the one-cell stage with the indicated mRNA. Injection of 100 pg of Wnt7a is associated with profound developmental defects ( $\ddagger$ ) precluding DRG development. (E) Dorsal views of 48 hpf WT and *wnt7aa<sup>-/-</sup>* *Tg(kdrl:GFP)* hindbrain cerebrovasculatures, with transgenic endothelial expression of Wnt7a, Wnt7a<sup>NTD</sup>, or Wnt7a<sup>K190A</sup>. BFP is used as a transgenesis marker, and Glut1 immunostaining to assess BBB differentiation. (F) Intracerebral (IC) hemorrhage score of 54 hpf *Tg(kdrl:GFP);Tg(gata1a:dsRed)* embryos treated from 34 hpf onwards with 1  $\mu$ M atorvastatin (ATV), with or without transgenic endothelial expression of Wnt7a<sup>K190A</sup>. Red arrowheads point to extravasated erythrocytes. (G) BBB leakage of Alexa Fluor 488 10 kDa Dextran upon ATV exposure in 54 hpf WT embryos. (H) Quantification of normalized brain parenchymal 10 kDa Dextran tracer intensity upon ATV exposure, with or without hemispheric transgenic endothelial expression of Wnt7a<sup>K190A</sup> in 54 hpf embryos. \*P<0.05; \*\*P<0.01; \*\*\*P<0.001; data represent mean  $\pm$  SD.

**Figure 4. Absence of ectopic Wnt activities or behavioral defects after brain-wide AAV-mediated gene delivery of Gpr124/Reck agonists in the mouse.**

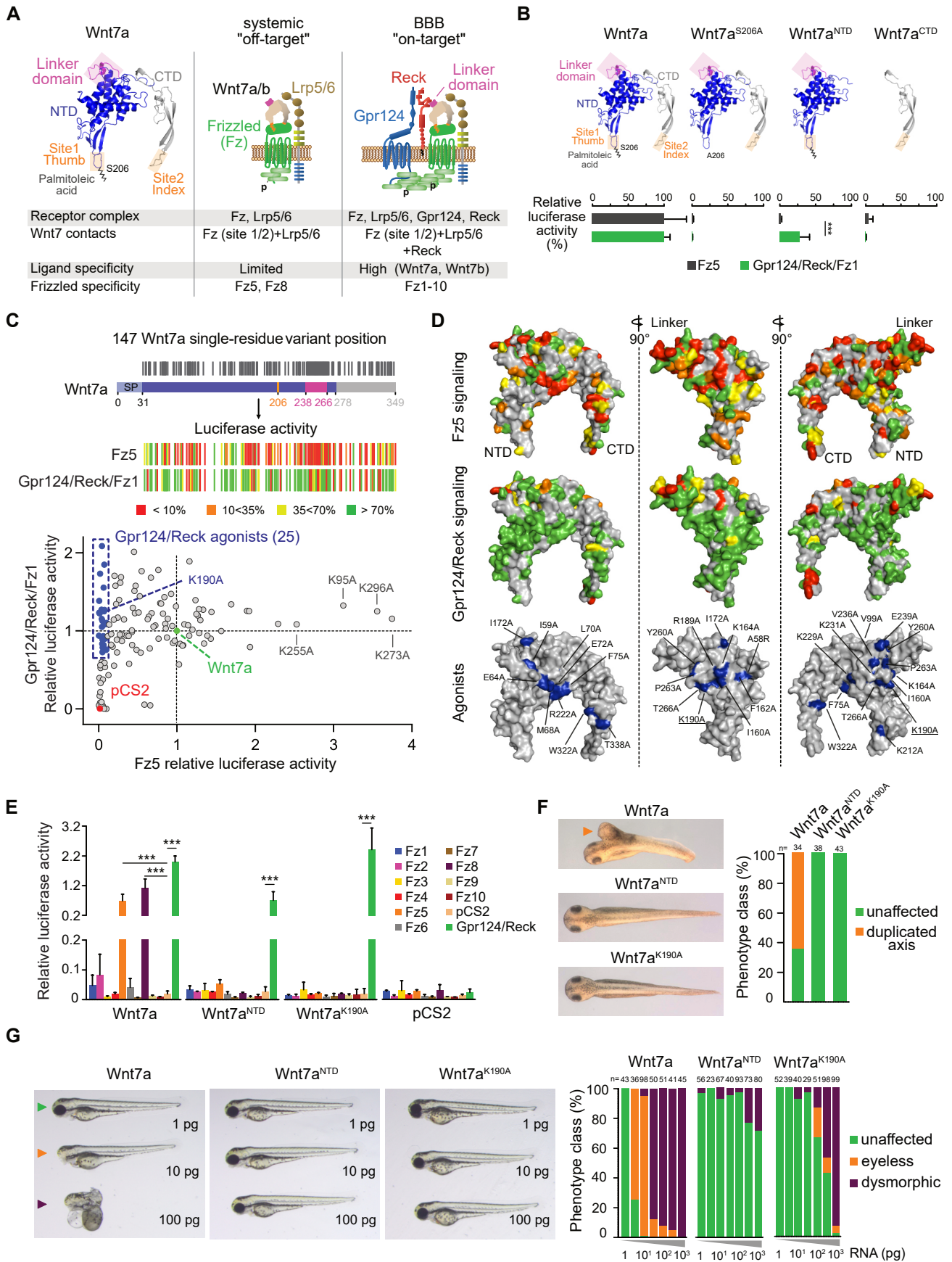
(A-B) Immunostaining of (A) sagittal brain sections for EGFP (green) and CD31-positive vessels (magenta, grey) and (B) coronal sections for CD31 (cyan, grey), Wnt7a (magenta, grey) together with a DAPI counterstain, two weeks after intravenous injections of the indicated AAVs. (C) Staining of coronal brain slices of AAV-injected BAT-GAL mice for LEF1 (green), lacZ (magenta, fire), laminin (cyan, white) and DNA (DAPI, blue), in the hippocampal area dorsal to the dentate gyrus (DG, left) and in the parafascicular nucleus area (PFN, right). Nuclear LacZ-positive cells or signal intensities were quantified at 7, 14, and 28 days post injection (dpi). HPF, hippocampal formation, TH, Thalamus; HY, hypothalamus, (D) RNAScope *in situ* hybridization of *Axin2* in coronal sections of AAV-injected WT mice at 14 dpi. (E) Spontaneous open field locomotor activity traces of P20 mice injected retro-orbitally at P2 with  $4 \cdot 10^{10}$  vg of the indicated AAV-PHP.eB viruses along with a group of uninjected control mice. Spontaneous locomotor activity is quantified as the total distance traveled for 3 min in the open field test. \* $<0.05$ ; \*\* $P<0.01$ ; \*\*\* $P<0.001$ ; ns: non-significant; data represent mean  $\pm$  SD.

**Figure 5. A single “hit-and-run” gene delivery of Gpr124/Reck agonists achieves neurovascular-specific Wnt/ $\beta$ -catenin activation and vessel normalization in glioblastoma multiforme**

(A) GL261-implanted mice, injected intravenously at 2 dpi (days post implantation) with AAVs, were imaged by MRI to evaluate *in vivo* tumor volume between 21 and 24 dpi. (B) At 25 dpi, mice were euthanized for endpoint gross morphology assessment (left) and H&E staining of serial sections (middle). Asterisks indicate hemorrhages (right). (C-G) Co-immunostaining of coronal tumor or parenchymal (parench) sections for endothelial cells (CD31, cyan) (C), vascular basement membranes (laminin, grey) (D), LEF1 (magenta) together with the endothelial nuclear marker ERG (cyan) (E), GLUT1 (magenta) together with laminin (cyan) (F), or fibrinogen (magenta) together with laminin (cyan) (G). (H) Correlation between endothelial Wnt activity (LEF1) and tumor volume, vessel density, BBB differentiation (GLUT1), and BBB leakage (fibrinogen extravasation) in tumors of AAV-EGFP mice (colored lines). (J) Same as (I) in AAV-K190A injected mice. \* $<0.05$ ; \*\* $P<0.01$ ; \*\*\* $P<0.001$ ; ns: non-significant; data represent mean  $\pm$  SD.

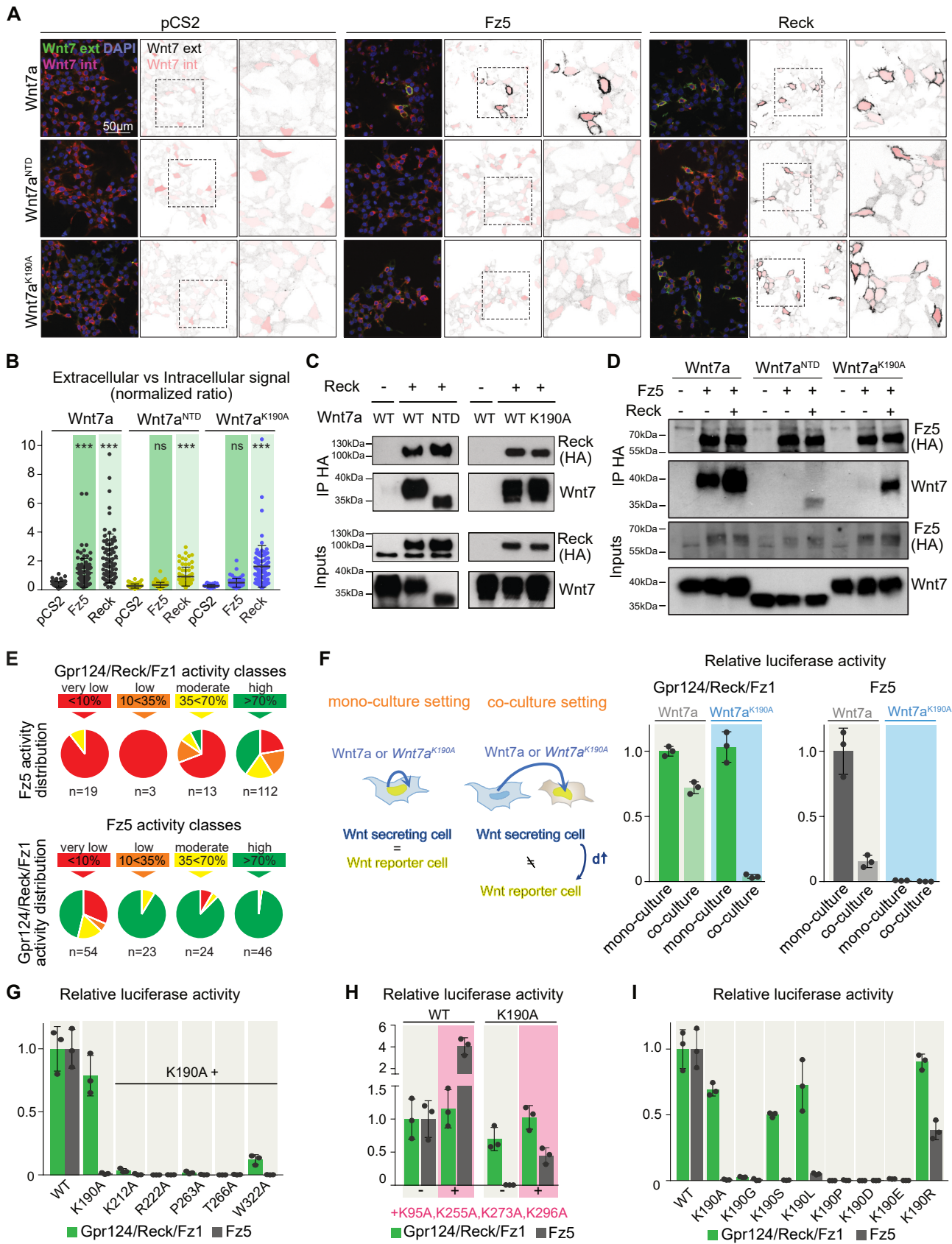
**Figure 6. Gpr124/Reck agonists as BBB repair agents in glioblastoma and stroke models**

(A) MRI monitoring of tumor volumes after implantation of  $1.10^5$  Tet-Off Dkk1 GL261 cells, in the absence of doxycycline (+Dkk1, -dox), or the presence of doxycycline (-Dkk1, +dox). Doxycycline-exposed mice were injected intravenously with AAV-EGFP or AAV-K190A, as indicated. (B) Quantification of fibrinogen leakage into the tumor. Data for WT GL261 are the same as in Fig. 5C (C) Representative images and quantification of leakage of transcidentally-perfused sulfo-NHS-biotin within the tumor (Tum.) and the healthy parenchyma (Par.). (D) Electron micrographs of tumor and cortical sections of HRP-injected mice. White and black asterisks indicate tracer within the vessel lumen and vascular basement membrane, respectively. Arrowheads label the junctions where the progression of the tracer within the intercellular cleft is blocked (E-G) Coimmunostaining of CD31 (cyan) together with Claudin-5 (magenta, grey) (E), Mfsd2a (magenta, grey) (F), or Desmin (magenta, grey) (G). (H-I) Infarct volumes of AAV-injected mice subjected to transient MCAO (H, TTC-stained sections), transient focal endothelin-1 stroke (I, ET-1, MRI scans) or permanent bengal rose photo-thrombotic stroke (I, PT, MRI scans). \* $<0.05$ ; \*\* $P<0.01$ ; \*\*\* $P<0.001$ ; ns: non-significant; data represent mean  $\pm$  SD.

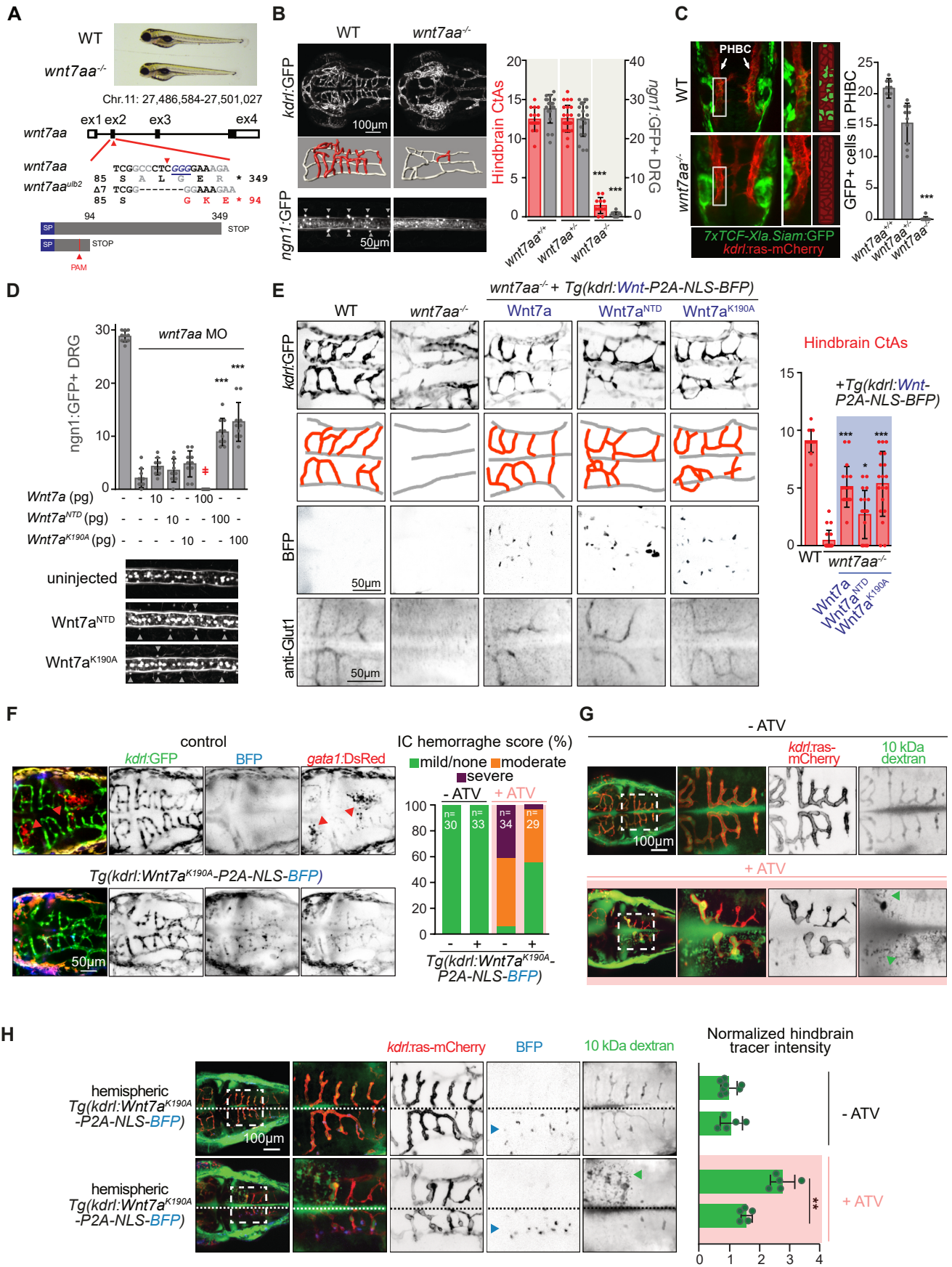


Martin et al., Figure 1



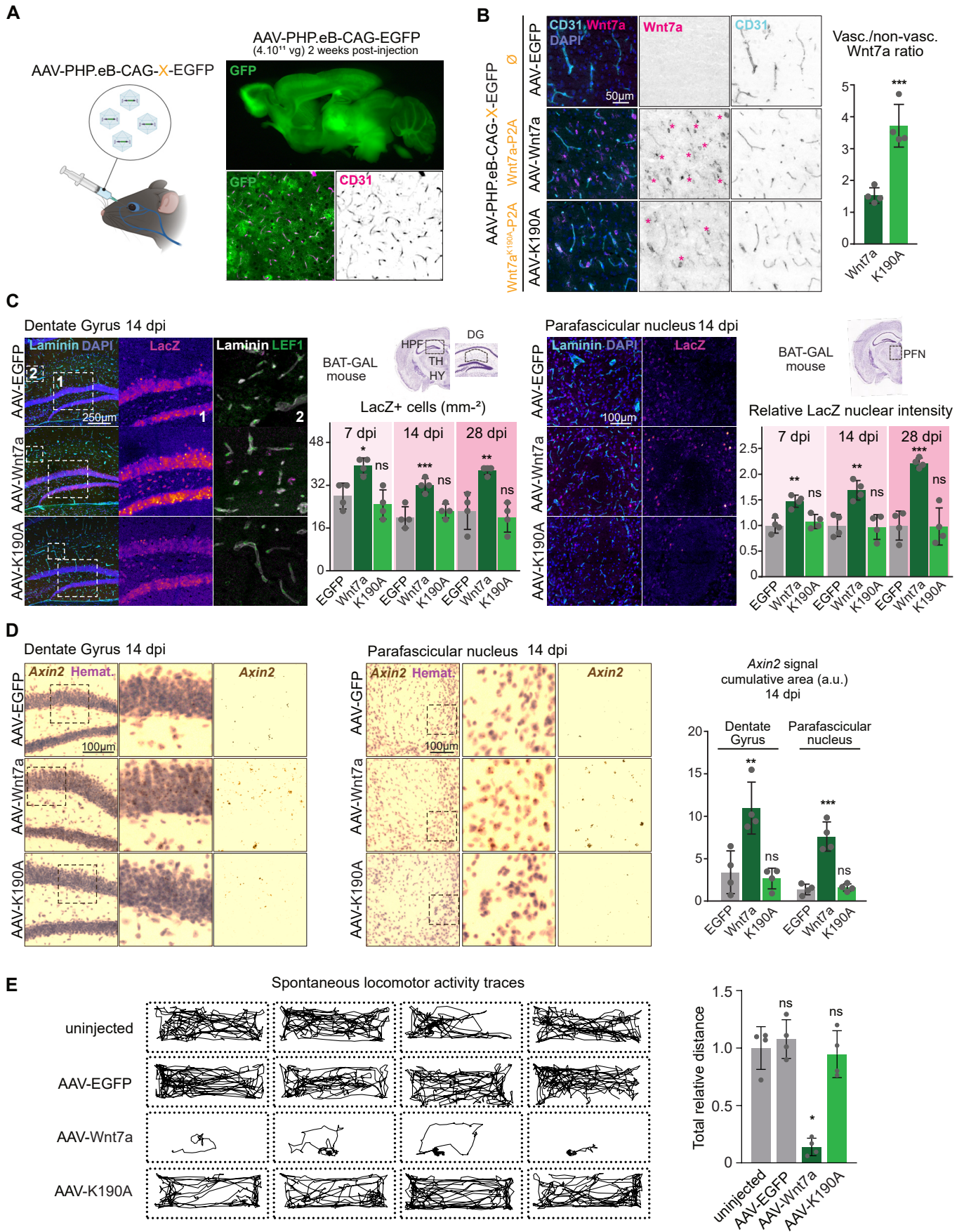


Martin et al., Figure 2

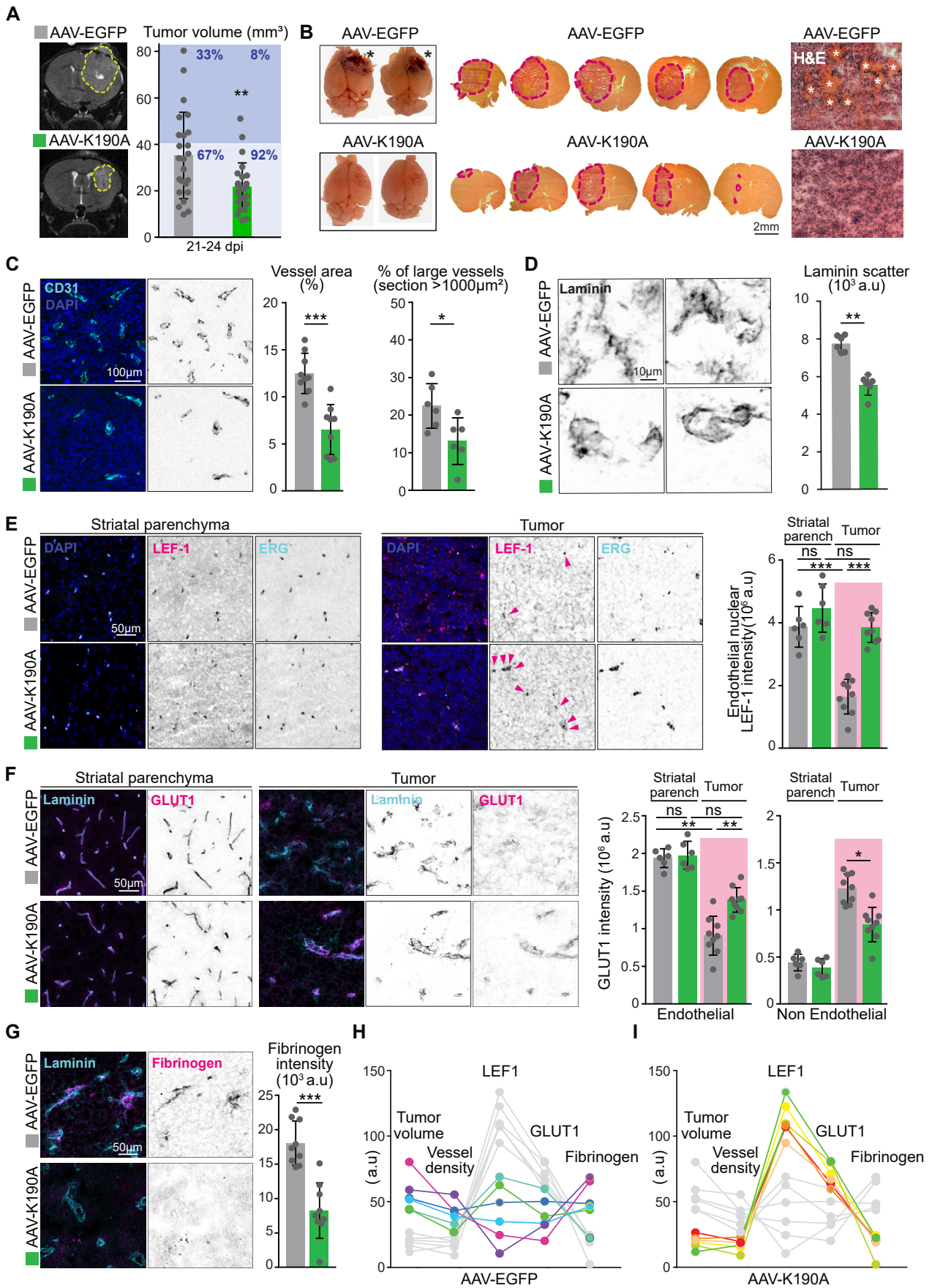


Martin et al., Figure 3



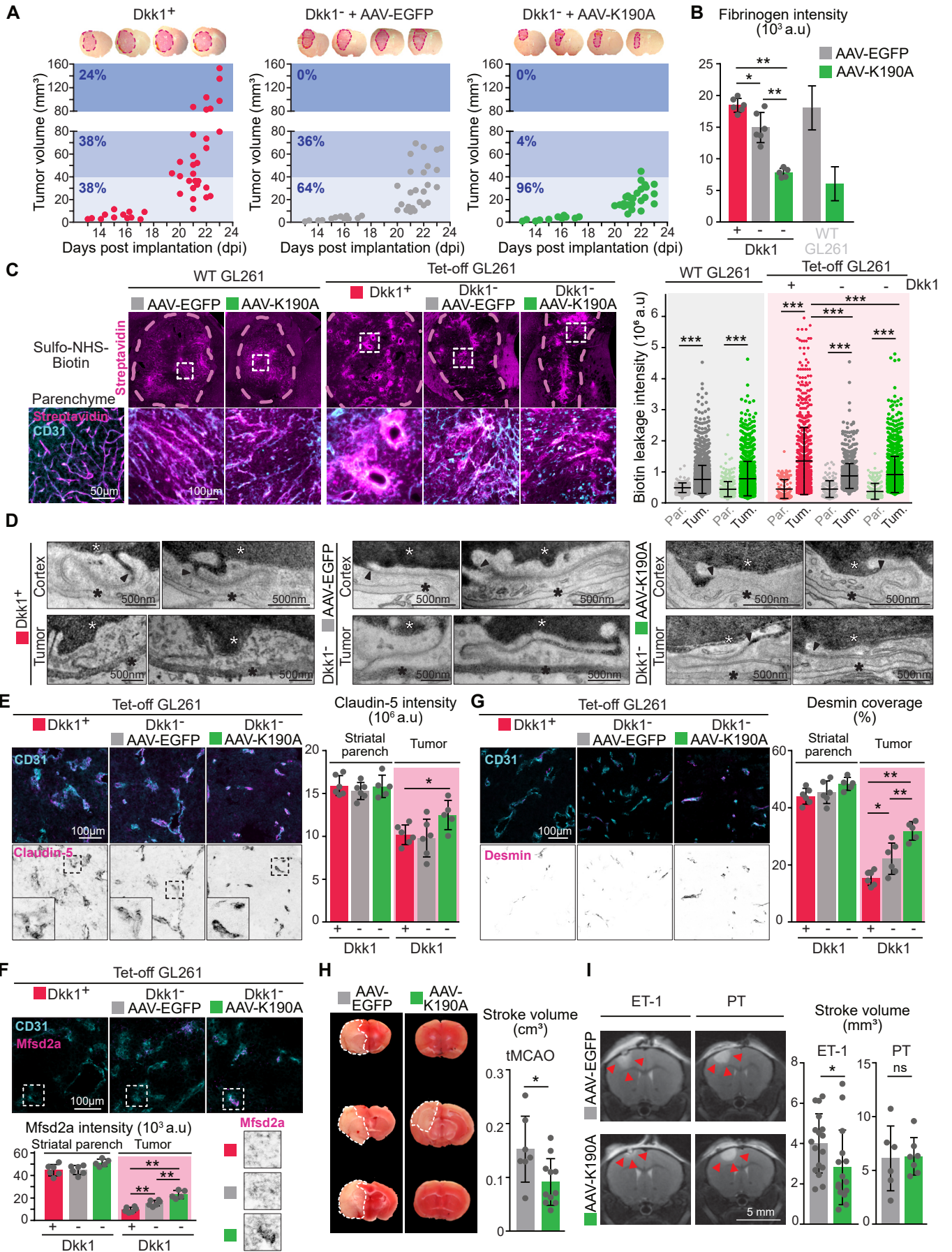


Martin et al., Figure 4



Martin et al., Figure 5





Martin et al., Figure 6



## Supplementary Materials for

Engineered Wnt ligands enable blood-brain barrier repair in neurological disorders

Maud Martin, Simon Vermeiren, Naguissa Bostaille, Marie Eubelen, Daniel Spitzer, Marjorie Vermeersch, Caterina P. Profaci, Elisa Pozuelo, Xavier Toussay, Joanna Raman-Nair, Patricia Tebabi, Michelle America, Aurélie de Groot, Leslie E. Sanderson, Pauline Cabochette, Raoul F.V. Germano, David Torres, Sébastien Boutry, Alban de Kerchove d'Exaerde, Eric Bellefroid, Timothy N Phoenix, Kavi Devraj, Baptiste Lacoste, Richard Daneman, Stefan Liebner, Benoit Vanhollebeke

Correspondence to: [Benoit.Vanhollebeke@ulb.be](mailto:Benoit.Vanhollebeke@ulb.be)

**This PDF file includes:**

Materials and Methods  
Figs. S1 to S21  
Tables S1 to S2

## Materials and Methods

### Constructs and antibodies

For Super Top Flash (STF) assays, the coding sequence of mouse Reck, Gpr124, Fz<sub>1-10</sub>, Lrp5, Wnt7a, and Wnt7b (and their variants), zebrafish Wnt7-aa, -ab, -ba, and -bb, Reck and Gpr124 were expressed from the CMV promoter of the pCS2+ or the pRK5 (for Fzs and Lrp5) plasmid. C-terminal V5-tagged single-residue and fusion variants of Wnt7a were obtained using In-Fusion cloning (ST0345, Takara) with tandem overlapping PCR products and were confirmed by Sanger sequencing. The NTD coding sequences correspond to amino-acids 1-278 of Wnt7a and Wnt7b, and the CTD part of the chimeric ligands to 279-360 (Wnt2), 281-351 (Wnt4), 310-380 (Wnt5a), 294-364 (Wnt6), 347-417 (Wnt10a), 284-354 (Wnt11), 294-364 (Wnt16) and 261-358 (XWnt8a). The collection of active human WNT-V5 ligands (Addgene #43807 to #43825 from the Xi He laboratory) was used in the Wnt/Fz pairwise STF experiments of Fig. S2. Firefly luciferase activities (derived from a genomic transgene in STF cells or ectopically expressed from the transfected M50 Super 8x TOPFlash plasmid, Addgene plasmid #12456 in other cells) were normalized to Renilla luciferase activities (pTK-Renilla vector transfection). For PLA (proximity ligation assay), IF (immunofluorescence) and IP (immunoprecipitation) experiments, pCS2+ plasmids coding for N-terminally HA-tagged mouse Reck and Fz5 were used together with the Wnt-V5 variants described above.

The following commercial primary antibodies were used in this study: mouse monoclonal antibody against V5 (R960-25, Thermo Fisher Scientific; RRID: AB\_2556564) at 1:400; rabbit polyclonal antibodies against Wnt7a (GTX128106, GenTex) at 1:300 for IF and 1:1000 for WB; purified rabbit polyclonal anti-HA antibodies (H6908, Sigma-Aldrich, RRID:AB\_260070) at 1:400 for PLA and 1:1000 for WB; rabbit polyclonal anti-Glut-1 (07-1401, Millipore, RRID:AB\_1587074) at 1:200 for mouse IF; rabbit polyclonal anti-Fibrinogen (ab34269, Abcam, RRID:AB\_732367) at 1:300; rabbit polyclonal anti-Mfsd2A (a gift from D. Silver,(65)) at 1:500, rabbit polyclonal anti-Desmin (ab15200, Abcam, RRID:AB\_301744) at 1300; rabbit monoclonal antibody against LEF-1 (2230, C12A5, Cell Signaling, RRID:AB\_823558) at 1:200; Alexa 647-conjugated rabbit monoclonal antibody against ERG (ab196149, Abcam) at 1:250; rabbit monoclonal antibody against Dkk1 (ab109416, Abcam, RRID:AB\_10861912) at 1:1000 ; rabbit polyclonal antibody against Claudin-5 (Thermo Fisher Scientific 34-1600 RRID:AB\_2533157) at 1:250 ; rabbit

monoclonal antibody against Caveolin-1 (3267, Cell Signaling Technology, RRID:AB\_2275453) at 1/200; rabbit monoclonal antibody against S100 $\beta$  (ab52642, abcam, RRID:AB\_882426) at 1:300; rabbit monoclonal antibody against Iba1 (ab178846, Abcam, RRID:AB\_2636859) at 1:300; biotin-conjugated rat monoclonal anti-HA (3F10, 12158167001, Roche, RRID:AB\_390915) at 1 ng. $\mu$ l<sup>-1</sup>; rat monoclonal anti-Laminin  $\gamma$ -1 (sc-65643, 3E10, Santa Cruz Biotechnology, RRID:AB\_1123687) at 1:500; rat monoclonal anti-CD31 (553370, BD Pharmingen, RRID:AB\_396660) at 1:250; rat monoclonal anti-GFAP (13-0300, Thermo Fisher Scientific, RRID:AB\_2532994) at 1:300; rat monoclonal anti- $\alpha$ -tubulin (MA1-80017, Pierce, RRID:AB\_2210201) at 1:2000; chicken polyclonal antibodies against  $\beta$  Galactosidase/lacZ (ab9361, Abcam, RRID:AB\_307210) at 1:200; chicken anti-GFP (GFP-1010, Aves Labs, RRID:AB\_2307313) at 1:400, guinea pig polyclonal antibodies against NeuN (ABN90, Merk, RRID:AB\_11205592) at 1:300. For additional detection of vessel and biotin we respectively used Isolectin GS-IB4 Alexa 594-Conjugate (I21413, Invitrogen) at 1:200 and Streptavidin Alexa 647-conjugate (S21374, Invitrogen) at 1:1000. For immunofluorescence we used Alexa 488-, Alexa 568- and Alexa 641-conjugated goat secondary antibodies (Molecular probes) at 1:400 and for western blotting we used HRP conjugated secondary antibodies (Promega) at 1:5000.

### **Cell CRISPR/Cas9 editing and culture**

HEK293T cells were obtained from ATCC (CRL-3216), and HEK293 STF cells were kindly provided by Jeremy Nathans (John Hopkins). They were grown in DMEM/F12 1:1 medium (Lonza) supplemented with 10% fetal bovine serum (Biowest, S1810) and maintained at 37°C in a humidified incubator equilibrated with 5% CO<sub>2</sub>. HEK293(T) cells were transfected with lipofectamine 2000 (Invitrogen) for STF assays or with Polyethylenimine (PEI max, Polyscience) for IP and IF at 70% confluency 24 h after plating. For staining experiments, HEK293(T) cells were seeded on poly-lysine (0.1 mg.ml<sup>-1</sup>) coated 12 mm coverslips. The CRISPR/Cas9-engineered *GPR124*<sup>-/-</sup>;*RECK*<sup>-/-</sup> mutant HEK293 STF line has been described before (29), together with the *FZ1-10*<sup>-/-</sup> HEK293T clone (29) used to build the *FZ1-10*<sup>-/-</sup>;*GPR124*<sup>-/-</sup>;*RECK*<sup>-/-</sup> HEK293T line. In order to generate the *RECK*<sup>-/-</sup> HEK293T and *FZ1-10*<sup>-/-</sup>;*GPR124*<sup>-/-</sup>;*RECK*<sup>-/-</sup> HEK293T cell lines, *GPR124* (5'-GCATCCGCTGGTACCACAAC-3') and *RECK* (5'-ATTGTTGATGGTCTCATCGA-3') CRISPR/Cas9 guide sequences were designed using the <http://crispr.mit.edu> website and cloned into pSpCas9(BB)-2A-GFP (66). The top 1% of GFP+



cells were isolated by FACS (AriaIII, BD Biosciences) 48 h after transfection and distributed in 96-well plates for clonal expansion and lesion determination by Sanger sequencing.

### **STF dual luciferase assay**

Dual luciferase assays were performed 2 days after transfection in 96-well plates using Dual-Luciferase Reporter Assay system (E1960, Promega) according to the manufacturers' protocol: after extraction in passive lysis buffer, the ratio of Firefly and Renilla luciferases activities of the cell lysates were measured. The co-culture assay was performed by seeding transfected reporter cells with Wnt7 ligands expressing HEK293T cells at a 1:1 ratio 1 day after transfection and 1 day prior to luciferase measurements. The amount of plasmid DNA transfected per well was optimized for each expression vector as follows: Renilla luciferase (0.5 ng), Wnt ligands (20 ng), Fz receptors (5 ng), Lrp5 (2.5 ng), Gpr124 (10 ng), Reck (10 ng). The total amount of DNA was adjusted to 100 ng per well with the empty pCS2 vector.

### **Proximity ligation assay**

The Duolink PLA technology (Sigma-Aldrich) was used to infer protein-protein interaction between HA-Reck and Wnt-V5 variants *in situ*. Two days after transfection, cells were fixed with 4% PFA for 10 min, blocked 30 min at 37°C with the Duolink blocking solution, incubated with primary antibodies anti-HA and anti-RECK for 1 h at RT, with anti-rabbit PLUS and anti-mouse MINUS PLA probes for 1 h at 37°C, with the Duolink Ligation solution for 30 min at 37°C and finally with the Duolink Amplification solution (Red) for 100 min at 37°C. Two PBS washes were included between each step. Slides were air-dried and mounted in ProLong Gold mounting medium supplemented with DAPI (Molecular probes). PLA signal was quantified using ImageJ. PLA-associated channel was thresholded to create a binary mask in which PLA dots were detected using the Particle Analysis plugin of ImageJ set to quantify the area and the mean signal intensity of each particle. Their Nearest Neighbor Distance (NND) was additionally computed using the ImageJ BAR plugin. To sort for membrane-localized signal, we filtered out the particles whose area was  $< 5\mu\text{m}^2$  or  $\text{NND} > 4\mu\text{m}$ . PLA signal was calculated per field of view as  $\frac{\sum_i A_i \times I_i}{N}$  where  $A$  is the area of the particle,  $I$  its mean intensity corrected for background and  $N$  the area fraction occupied by the nuclei signal in the field (measured on DAPI thresholded pictures), indicative of the number of cells.

### **Surface and intracellular immunofluorescence staining**

Two days after transfection, *GPR124<sup>-/-</sup>;RECK<sup>-/-</sup>* HEK293 cells were blocked in PBS/BSA 2% for 20 min at 4°C, incubated with primary antibody against Wnt7a for 1 h at 4°C, fixed in 4% paraformaldehyde for 10 min at RT, permeabilized with 0.1% saponin in PBS for 5 min, blocked again in PBS/BSA 2% for 1 h and sequentially incubated with primary anti-V5 and Alexa-conjugated secondary antibodies for 1 h at RT. Antibodies were diluted in PBS/BSA 2% and cells were washed three times with PBS after each step. Membrane accumulation of the ligand was quantified using ImageJ as follows: maximum intensity projection of the signal obtained after permeabilization (V5 intracellular signal) was used to detect expressing cells and to measure their mean signal intensity. For each cell, the Z plane associated with the strongest membrane-associated signal (Wnt7 extracellular signal) was used to measure its mean signal intensity along a line of circa 2 µm width (30 pixels) along the cell surface. We also included in this analysis cells that were only positive for membrane signal. The ratio between extracellular and intracellular signals after background correction was calculated per cell, normalized to the ratio corresponding to a double negative cell in the same field of view and averaged per field.

### **Co-Immunoprecipitation, dot blot, and western blot**

For co-immunoprecipitation experiments, *RECK<sup>-/-</sup>* HEK293T were incubated with the membrane-impermeable crosslinker DTSSP (3,3'-dithiobis(sulfosuccinimidyl propionate), Sigma-Aldrich) at 0.2 mM in HBS (20 mM HEPES, pH 7.4, 150 mM NaCl, 1 mM CaCl<sub>2</sub>, 0.5 mM MgCl<sub>2</sub>) for 2 h at 4°C, two days after transfection in 6-well plates. After quenching the reaction with 50 mM Tris/HCl, pH 7.4 for 15 min, total cell extracts were prepared in RIPA buffer (10 mM Tris-HCl pH 8, 150 mM NaCl, 1% Triton X-100, 0.5% sodium deoxycholate, 0.1% SDS, protease inhibitor cocktail (Complete - Roche)) under rocking at 4°C for 30 min. Extracts were cleared by centrifugation (15 min at 14,000 rpm) and incubated, after saving 10% as input control, for 2 h at 4°C with a biotin-conjugated antibody against HA and for 1 h at 4°C with high capacity streptavidin agarose beads (Pierce) under constant rotation. Beads were washed four times with RIPA buffer and boiled for 10 min in 2X Laemmli sample buffer containing 15% β-mercaptoethanol. Input protein extracts and bead eluates were analyzed by SDS-PAGE and Western blotting, according to standard procedures and developed by autoradiography with ECL

Plus substrate (PerkinElmer) after incubation with primary and secondary antibodies respectively for 1 night and 1 h at 4°C. Dot blot analysis was performed to assess ligand secretion. Cellular supernatant was collected 2 days after transfection, cleared by centrifugation, and transferred to a nitrocellulose membrane (GE Healthcare) using a BioDot SF apparatus (Bio-Rad). The membrane was then processed as described above. For *in vitro* analysis of Dkk1 expression in Tet-off GL261 cells, cells were cultured in the absence or presence of doxycycline (0.002 to 2 µg.ml<sup>-1</sup>) for 48 h before extraction in RIPA buffer. To analyze *in vivo* expression levels, tumors were dissected at 21 dpi from mice fed with control or doxycycline-containing diet (1 g.kg<sup>-1</sup> doxycycline hyclate, Safe Diets, France).

### ***Structural modeling***

The mouse Wnt7a structure was modeled based on the crystal structure of Xenopus Wnt8a in complex with mouse Fz8 CRD (PDBID:4F0A) (20) as described previously (29).

### ***Animal procedures - zebrafish***

The transgenic and mutant lines used in this study are *Tg(kdrl:EGFP)<sup>s843</sup>* (67), *Tg(kdrl:HRAS-mCherry)<sup>s896</sup>* (68), *Tg(7xTCF-Xla.Siam:GFP)<sup>ia4</sup>* (69), *Tg(-17.0neurog1:EGFP)<sup>w61</sup>* (70), *Tg(gata1a:dsRed)<sup>sd2</sup>* (71) and *gpr124<sup>s984</sup>* (27). Zebrafish (*Danio rerio*) were maintained at 28°C on a 14 h light/10 h dark cycle. Embryos were obtained and raised under standard conditions in accordance with European and national ethical and animal welfare guidelines (protocol approval number: CEBEA-IBMM-2017-22:65). The *wnt7aa<sup>ulb2</sup>* allele was generated using the CRISPR/Cas9 technology (72). The targeting sgRNA construct was cloned into pT7-gRNA (Addgene plasmid #46759) using these primers: *wnt7aa-fwd* 5'-TAGGTGGAAGCTGCTCGGCCCTC-3', *wnt7aa-rev* 5'-AAACGAGGGCCGAGCAGTTCCA-3'. sgRNA was transcribed from pT7-gRNA using the MEGAshortscript T7 transcription kit (Ambion) and injected at 50 pg into one-cell stage embryos, together with 150 pg of nls-zCas9-nls mRNA transcribed from pT3TS-nCas9n (Addgene plasmid # 46757) using the mMessage mMachine T3 Kit (Ambion).

### ***Morpholinos, RNA, and DNA constructs microinjection***

4 ng of the following *wnt7* splice-blocking morpholinos (GeneTools) were injected into one-cell stage embryos: *wnt7aa*: TTCCATTTGACCCTACTTACCCAAT, *wnt7ab*: AACCCCTACAAATGACCACAGAACT, *wnt7ba*: AAGCATTCGCTCAAACCTACAGGTA, *wnt7bb*: ACAGATTGAAACACTTACAGGTAGC. Synthetic mRNAs were transcribed from pCS2 plasmids after NotI digestion using the mMessage mMachine SP6 Kit (Ambion) and injected into one-cell stage zebrafish embryos at the concentration indicated in the Figures. Transient mosaic endothelial over-expression was obtained by co-injection of 10 pg of Tol2 transposase mRNA and 10 pg of the *pT2-kdrl-mWnt7a(WT, K190A or NTD)-P2A-NLS-eBFP* DNA constructs.

### ***Whole-mount in situ hybridization (WISH)***

Whole-mount in situ hybridization was performed as described previously (73). Embryos were hybridized with digoxigenin-labeled riboprobes using the following primers: *wnt7aa*-fwd: 5'-GGGGATTATTTATTTGAAGATTGG-3'; *wnt7aa*-rev: 5'-TAATACGACTCACTATAGGGGTGCATCTAGGAAGACCTTTGAG-3'; *wnt7ab*-fwd: 5'-CATGACAATGGCTGGAAATG-3'; *wnt7ab*-rev: 5'-TAATACGACTCACTATAGGGGCCACACACGTGAATACTGG-3'; *wnt7ba*-fwd: 5'-GCATCAACGAGTGCCAGTATCAG-3'; *wnt7ba*-rev: 5'-TAATACGACTCACTATAGGGCATCCACGAAGCGTCTGGAGAAC-3'; *wnt7bb*-fwd: 5'-GAGTTCTCACGGAAGTTTGTGGATG-3'; *wnt7bb*-rev: 5'-TAATACGACTCACTATAGGGTTGAACCGCTTTGTTGTACTTGTCC-3'. Probes were transcribed with T7 RNA polymerase (Roche) and detected using anti-DIG AP (1:5000) and NBT/BCIP substrate (Roche). Embryos were sectioned (Vibratome, 50 µm) after embedding in 4% ultrapure low melting point agarose (Thermo Fisher Scientific).

### ***Phenotyping***

Staging was performed according to Kimmel et al. (74). CtAs, DRG neurons and TCF-positive endothelial cells were quantified on confocal Z-stack recordings of live, anesthetized (low doses of tricaine), agarose-embedded (1% low melting point agarose) transgenic zebrafish. For hemorrhagic stroke experiments, *Tg(kdrl:EGFP);Tg(gata1a:dsRed)* embryos were treated from 34 hpf onwards with 1 µM atorvastatin (Sigma-Aldrich). Embryos were graded based on the extent of intracerebral bleeding under a bright-field stereoscope. For that purpose, brains were arbitrary

divided into 4 areas (left and right, forebrain/midbrain and hindbrain) in which the level of hemorrhages was scored in a double-blind manner as 0 (no hemorrhage), 1 (small hemorrhage) or 2 (large hemorrhage). The phenotype was considered as mild if the cumulated score of the 4 zones was  $\leq 1$ , moderate if it was  $\leq 4$  and severe if it was  $> 4$ . Confocal pictures were taken for illustration. Tracer leakage assays were performed by micro-injection of 1 nl of  $10 \text{ mg.ml}^{-1}$  Alexa Fluor 488 Dextran 10.000 MW (Invitrogen) in PBS in the common cardinal vein at 54 hpf. Embryos were mounted dorsoventrally and individually imaged at 30 min post-injection using a Zeiss LSM900 inverted laser scanning microscope. Quantification was performed using ImageJ by generating maximum intensity projection of stack volumes around  $20 \mu\text{m}$  thick, including the dorsal arch of the CtAs about  $40 \mu\text{m}$  above the PHBC. Projections were positioned minimally  $15 \mu\text{m}$  below the dorsally located ventricle to avoid fluorescence signal contamination from tracer accumulated in this structure. Mean fluorescence intensity was calculated in the area covering the hindbrain parenchyma. The relative fluorescence intensity was determined by dividing the mean parenchymal tracer intensity by the maximal intensity of the tracer signal in the CtA lumen.

### ***Whole-mount Immunostaining***

A custom polyclonal rabbit antibody was generated against zebrafish Glut1/Slc2a1a (Eurogentec, Belgium). Two KLH-MBS-conjugated peptides (Slc2a1a 45-59: NETWHNRYSEYIPPT and 471-485: ADKYNRDDLNTLGAD), designed to minimize cross-reactivity with the paralogue Slc2a1b, were used for immunization. For Glut-1 immunostaining, manually dechorionated zebrafish embryos were fixed with 4% paraformaldehyde overnight at  $4^\circ\text{C}$ , permeabilized with  $20 \mu\text{g.ml}^{-1}$  Proteinase K in PBS 0.5% TritonX-100 for 30 min at  $37^\circ\text{C}$ , fixed again with 4% paraformaldehyde 20 min at RT, blocked 1 h at RT with 10% normal goat serum, 0.5% TritonX-100, 1% DMSO in PBS and sequentially stained overnight at  $4^\circ\text{C}$  with primary and secondary antibodies diluted in blocking solution. Embryos were washed several times with PBS 0.5% TritonX-100 for 5 min after each step and for 30 min after the staining steps.

### ***Animal procedures - Xenopus***

*Xenopus laevis* embryos, obtained from adult frogs by hormone-induced egg-laying and *in vitro* fertilized using standard methods according to Nieuwkoop and Faber (1967), were microinjected with 15 pg mRNA of Wnt7a variants into the ventral vegetal region of four-cell stage embryos.

Experiments were conducted in accordance with European and national ethical and animal welfare guidelines (protocol approval number: CEBEA-IBMM-2017-22:19)

### ***Animal procedures - Mouse***

WT C57BL/6 (Charles River Laboratories) and transgenic BAT-gal ( $\beta$ -catenin-activated transgene driving expression of nuclear  $\beta$ -galactosidase reporter) mice (41) were used in this study. Animals were housed under standard conditions and fed ad libitum. All animal handling was performed to minimize suffering. Experimental protocols were conducted in accordance with European and National regulations and guidelines. Protocol approval numbers: CEBEA-IBMM-2019-24:104 (ULB), FK10/1052 (Goethe University Frankfurt), S14044 (UCSD), CMM-2865 (Ottawa Hospital Research Institute).

### ***AAV injection***

Recombinant PHP.eB AAV particles were produced and purified from HEK293T cells at the Viral Vector Facility (VVF) of the Neuroscience Center Zurich (ZNZ) from the pAAV-CAG-EGFP and pAAV-CAG-mWnt7a (WT or K190A)-2A-EGFP vectors. Mouse neonates (2 days old) were injected retro-orbitally with 50  $\mu$ l of a PBS suspension containing  $4 \cdot 10^{10}$  vg of AAV vector packaged into the PHP.eB capsid. 8-week old mice were injected intravenously in the tail (or retro-orbitally in the case of behavioral testing) with  $0.4\text{-}1 \cdot 10^{12}$  vg of PHP-eB AAV capsids in 200  $\mu$ l PBS.

### ***Locomotor activity of neonatally-injected mice***

Locomotor activity was recorded by videotracking at P20, 18 days after AAV injection. Pools of four mice were familiarized for 10 min in open field locomotor activity boxes (14 cm  $\times$  36 cm) before being recorded for 3 min. Horizontal ambulation was analyzed at 3 Hz using the Manual Tracking plugin from ImageJ. The cumulated travelled distance was calculated and normalized to the non-injected condition.

### ***Adult mice behavioral studies***

Three weeks after viral injection, mice were tested in the open field, rotarod, nestlet shredding, marble burying, and Y-maze behavioral assays after having been acclimated to the behavior room for 30 min.

**Marble Burying.** Twenty marbles were arranged 4x5 in an evenly spaced grid on top of approximately 3 cm of packed fresh bedding in a standard-sized cage. A mouse was placed in a corner of the cage and left for 30 min. The number of marbles that remained unburied was quantified by a researcher blind to the experimental condition. A marble was considered “buried” if 1/3 or less of it was visible.

**Rotarod.** Mice were placed on the rotarod (PanLab, Harvard Apparatus) and remained at a speed of 4 rpm for a 30 sec acclimation period. Mice that fell off the rod during this acclimation period were placed back on. The rotarod accelerated from 4 rpm to a max speed of 40 rpm over 300 sec. The latency to fall was recorded, and each mouse was returned to its home cage after falling. Three trials were performed each day for 5 consecutive days, with a 1.5 min resting period between each trial. The latency to fall was averaged across the 3 trials for each day.

**Open Field.** A mouse was placed in the center of an open field arena. The arena (50.8 cm x 50.8 cm) had white Styrofoam walls (30.5 cm high) and a plexiglass floor placed over a piece of white cardboard. Lines on the cardboard demarcated a square “inner zone” (35.5 cm x 35.5 cm) within the arena. The mouse was filmed for 10 min while the experimenter remained out of sight. The middle 5 min (2:30 – 7:30) was used for quantification. The duration the mouse spent in the inner and outer zone were quantified by a researcher blind to the experimental condition.

**Nestlet Shredding.** Nestlets were pre-weighed with an analytic scale before the experiment. Each mouse was placed in a clean cage with one nestlet and left alone for 1 h. All nestlets were allowed to dry overnight. Extra cotton and bedding was carefully removed from each nestlet by a researcher blind to experimental condition, and the nestlets were again weighed on an analytical scale. The ratio of nestlet shredded was calculated by dividing the remaining nestlet mass by its original mass.

Y-maze. Mice were housed in a 12 h light/dark cycle, and the Y-maze protocol assessing spatial reference memory (75) was performed during the light period of the day under a luminosity of 20 Lux. The Y-maze consisted of a white maze with three 50 cm long arms intersected at 120°. Visual clues were displayed at each end of the arms. For the first part of the protocol, one of the arms was closed off with a divider. A mouse was then placed in the maze and allowed to explore the two open arms for 15 min. After 20-25 min back in its home cage, it was placed in the same starting arm that was used in the training phase and was allowed to explore the three arms of the maze (including the novel arm) for 5 min. Mice were video-tracked using EthoVision XT equipment (Noldus Technology), and the distance traveled in each arm was calculated.

### ***Glioblastoma model***

Mouse GL261 glioblastoma cells (DSMZ no. ACC 802) were cultured in DMEM-GlutaMAX-I medium (Invitrogen) containing 10% fetal bovine serum (Biowest, S1810). The previously generated Dkk1 Tet-Off GL261 cells (76) were cultured in the same media supplemented or not with 1  $\mu\text{g}\cdot\text{ml}^{-1}$  doxycycline for 5 days before implantation.

For intracerebral tumor implantations, anesthetized mice were placed into a stereotactic device and 2  $\mu\text{l}$  of PBS containing  $10^5$  living GL261 cells were injected at  $0.25 \mu\text{l}\cdot\text{min}^{-1}$  into the striatum using the coordinates relative to bregma: 0.5 (anterior-posterior), 2 (mediolateral), and 3.5 (dorsoventral) using a Hamilton Microliter #75N injection syringe with a 26Ga needle. The needle is left in place for at least 2 min before being slowly removed. At the end of the procedure, the incision was sutured and mice were allowed to recover two days before being injected with AAVs. Alternatively, mice were injected with AAVs 2 weeks before GL261 cell implantation. For Tet-Off-dependent experiments, mice were fed with control or 1  $\text{g}\cdot\text{kg}^{-1}$  doxycycline hyclate containing diet (Safe Diets, France) starting 2 weeks before implantation until the end of the experiment. Mice were individually monitored at 7, 14 and/or 21 days post implantation (dpi) using Magnetic Resonance Imaging (MRI) performed on a 9.4T Biospec or on a 1T ICON operating under Paravision 5.1 software (Bruker). MR signal was obtained using a mouse head transmit/receive volume coil (23 mm inner diameter). Animals were anesthetized in a chamber with isoflurane (2.5-3%) vaporized in oxygen ( $2 \text{ L}\cdot\text{min}^{-1}$ ) and were transferred to a dedicated imaging cradle, in which isoflurane delivery was adapted (1.5-2% in  $0.4 \text{ L}\cdot\text{min}^{-1}$  oxygen flow). Their body temperature was



maintained by warm water circulating in a blanket, and their respiratory rate was monitored during the whole imaging session, in accordance with CMMI protocol number 2011- 07 (LA1500589). A T2-weighted 2D TurboRARE (Rapid Acquisition with Relaxation Enhancement) sequence was used to visualize the brain on 15 slices (0.5 mm thickness (no gap), 83 microns plane resolution, repetition time (TR): 3000 ms, effective echo time (TE): 60 ms, number of averages: 16, acquisition time: 9 min 36 sec, fat saturation). Tumors were manually contoured on each slice by drawing region of interest (ROI), from which volumes were obtained with the VivoQuant software (InviCRO, version 2.0). For histology, mice were euthanized at 25 dpi and brains were embedded into OCT before freezing at -80°C. For sulfo-NHS-biotin permeability assay, anesthetized mice were perfused intracardially at 22-24 days post implantation with 10 ml of 0.5 mg.ml<sup>-1</sup> EZ-Link-Sulfo-NHS-Biotin (Thermo Fisher Scientific, 21217) followed by 10 ml of 1% PFA/PBS at a flow rate of 2-2.5 ml.min<sup>-1</sup>. The dissected brains were fixed overnight in 4% PFA/PBS at 4 °C before being rinsed in PBS, embedded in 4% agarose and cut in 50 µm thick sections using a vibratome. Floating sections were blocked/permeabilized in PBS 0.5% TritonX-100, 10% normal goat serum for 2 h at RT, incubated with primary antibodies against CD31 overnight at 4°C and 4 h at RT, with secondary antibodies additionally containing Alexa 647-conjugated streptavidin 2 h at RT, with five PBS 0.1% TritonX-100 washes after each staining step. After PBS and distilled water washes, sections were mounted in Dako medium (Agilent).

### ***Transient MCAO (tMCAO) stroke model***

MCAO surgeries were performed 15 days after AAV injection as described previously (77). The operator was blinded to treatment of mice. Mice were anesthetized with 1.5 % isoflurane followed by right MCA occlusion using standardized monofilament (0.23 mm tip diameter, Docol) for 60 min. Stroke incidence was in the range of 80–90 % and animals were only excluded when there was no stroke based on TTC staining. More than 80 % of animals survived MCAO surgery. The cerebellum and olfactory lobes were removed from isolated mouse brains that was then cut into 2 mm-thick slices on a brain matrix. Three brain slices per animal were stained with 2,3,5-triphenyltetrazolium chloride (TTC, 2 %) to outline infarcts and measure stroke volume as previously described (78).

### ***ET-1 and PT stroke models***

For photothrombosis (PT) stroke induction, mice received an intraperitoneal injection of the light-sensitive dye Rose Bengal (RB, 100 mg.kg<sup>-1</sup>, MilliporeSigma: Cat. No. R3877) while placed in a stereotaxic frame. RB was allowed to circulate for 5 min, and a laser (530 nm, 20 mW) was placed 3 cm from the skull surface above the motor cortex at the following coordinates from bregma: +0.7 anterior-posterior (AP), +2 medial-lateral (ML). The laser was left ON for 10 min, activating RB and in turn causing platelet aggregation and blood clot formation (15, 16). For endothelin-1 (ET-1)-induced stroke, after incising the scalp, a small burr hole (~1.0 mm diameter) was drilled in the skull and 1 µl of ET-1 (800 pmol, Abcam: Cat. No. ab120471) was stereotaxically injected in the motor cortex (from bregma: +0.7 AP, +2 ML, -0.4 DV) at a rate of 0.1 µl.min<sup>-1</sup> with a syringe pump. For both PT and ET-1 strokes, mice were initially anesthetized with 5% v/v oxygen and isoflurane, which was subsequently reduced to 2% v/v for the duration of the procedure. Internal body temperature was maintained at 37°C ± 1°C for the entire procedure. All mice received subcutaneous buprenorphine (0.1mg/kg, Ceva Animal Health: Vetergesic® buprenorphine hydrochloride) following stroke induction for analgesia. Infarct volume quantification: *in vivo* magnetic resonance imaging (MRI) was performed 48 h after stroke induction using a 7 Tesla GE/Agilent MR (University of Ottawa pre-clinical imaging core facility). Mice were anesthetized for the MRI procedure using 2% v/v oxygen and isoflurane. A 2D fast spin echo sequence (FSE) pulse sequence was used for the imaging, with the following parameters: slice thickness=0.5 mm, spacing=0 mm, field of view=2.5 cm, matrix=256x256, echo time=41 ms, repetition time=7000 ms, echo train length=8, bandwidth=16 kHz, fat saturation. Stroke lesions demonstrated hyperintensity. MRI images were loaded in the Fiji software and infarct volumes were quantified using a custom script for outlining the infarct perimeter. All infarct volumes were quantified twice to obtain an average of the two measures for each animal.

### ***Mouse brain histology and immunostainings***

Serial coronal sections of 12 µm were prepared on native brain using a cryostat (Leica). Brain slices were mounted on SuperFrost slides (Thermo Fisher Scientific) and were submitted to H&E (Hematoxylin and Eosin) staining following standard procedures to assess the anatomical tumor localization and size. For immunostainings, native brain sections were fixed in 4% paraformaldehyde for 10 min at RT, washed 2 times with PBS, blocked in PBS 0.1% TritonX-100, 10% normal goat serum for 1 h at RT, incubated with primary antibodies overnight at 4°C and

with secondary antibodies 2 h at RT, with 5 PBS 0.1% TritonX-100 washes after each staining step. Antibodies were diluted in the blocking solution and DAPI ( $1 \mu\text{g}\cdot\text{ml}^{-1}$ ) was added to the secondary antibodies. Slides were mounted in DAKO medium (Agilent) and imaged using a confocal microscope. LacZ and LEF-1 immunostainings were used to assess  $\beta$ -catenin activity in brain from BAT-Gal mice after AAV injection. Staining was performed on similarly located sections and the number of lacZ or LEF-1 positive nuclei (co-localizing with DAPI signal) were counted. For the analysis of lacZ in the hippocampus, a  $0.25 \text{ mm}^2$  area dorsal to the dentate gyrus was analyzed, whereas a  $0.5 \text{ mm}^2$  area centered around the parafascicular nucleus was used to quantify the intensity of lacZ signal in this region of the thalamus. The distribution of EGFP expression upon AAV gene delivery was quantified by measuring of the percentage of the area occupied by the thresholded signals of vessels (CD31 or isolectin), astrocytes (GFAP) and neurons (NeuN) that is also positive for EGFP. For pericyte co-localization assessment, three-color-intensity profiles along a line were made using the 'plot profile' option in ImageJ for each channel (EGFP, Desmin, CD31). Tumor vessel phenotypes were analyzed on slides from the center of the tumor. Quantifications were performed using ImageJ on maximum intensity projections from 5 different fields of view and averaged per mouse. For analysis of vessel coverage, thresholded pictures of CD31 staining were used to measure the portion of the area occupied by vessels (area fraction measurement option). Laminin dispersion was calculated as  $\text{SD}_i/\sqrt{i}$  in which  $\text{SD}_i$  is the standard deviation of intensity and  $i$  the mean intensity of the signal. For LEF-1 expression analysis, thresholded DAPI, ERG and laminin signals were used to isolate endothelial and non-endothelial nuclei using the Particle Analysis plugin. Endothelial specific mean signal intensity of LEF-1 in nuclei was measured and normalized to the nuclear LEF-1 signal outside of the vessels after background subtraction. Quantification of Claudin-5, Mfsd2A and Caveolin-1 endothelial expressions were performed by detecting vessel structures using the Particle Analysis plugin on thresholded CD31/laminin pictures and measuring their mean respective signal intensity after background subtraction. The same procedure was used to measure GLUT1 mean endothelial intensity per surface unit and this value was multiplied by the cell area (vessel area divided by the number of nucleus) to get the total GLUT1 signal per cell. For assessing fibrinogen leakage, the detected vessel areas were scaled up by 125% before measuring fibrinogen intensity in this area. For analysis of pericyte coverage, the ratio between the area of the thresholded desmin and CD31 signals was calculated. Sulfo-NHS-Biotin leakage was quantified as the intensity of the

streptavidin signal in the area around the vessel after background subtraction. This area was defined as the region corresponding to a 150% scale up of the thresholded CD31 signal from which the initial vessel area was subtracted. Only vessels whose inside streptavidin signal was bigger than the background were taken into account.

### ***Mouse brain RNAScope in situ hybridization***

Whole brains were fixed overnight with 4% PFA at 4°C before being embedded into OCT, frozen at -80°C and sliced using a cryostat (Leica) into serial coronal sections of 12 µm mounted on SuperFrost slides. Sections were submitted to RNAScope® procedure with the brown detection kit (ACD-Biotechne) according to manufacturer instructions and using *axin2* probe (#400331). After post-fixation with formalin for 30 min and dehydration in ethanol, slides were baked at 60°C for 30 min using an HyBEZ Oven. They were then covered with the RNAScope Hydrogen Peroxidase solution for 10 min at RT, before 5 washes in distilled water. Epitope retrieval was achieved with the RNAScope Target Retrieval Reagent for 15 min at 100°C and sections were let to dry at 60°C. Tissues were then submitted to a series of incubation at 40°C in the HyBEZ Oven followed by two washes in RNAScope Wash Buffer 1X: 15 min with the Protease Plus solution, 2 h with the probe, 30 min with the APM1 solution, 15 min with the APM2 solution, 30 min with the APM3 solution, 15 min with the APM4 solution. The two last amplification steps were performed at RT: 30 min with the APM5 solution and 15 min with the APM6 solution. Sections were stained with a 1:1 ratio of RNAScope DAB-A and DAB-B solutions for 10 min at RT and counterstained with 50% Hematoxylin for 2 min at RT before dehydration and mounting.

### ***Mouse brain transmission electron microscopy***

Mice were retro-orbitally injected with 10 mg HRP (Sigma-Aldrich) in 200 µl of PBS that was let to circulate 30 min. After cervical dislocation, brains were harvested and fixed in 2% glutaraldehyde/4%PFA in 0.1 M cacodylate buffer for 1 h at RT followed by 5 h at 4°C. Brains were embedded in 4% agarose in 0.1 M cacodylate buffer and cut in 50 µm thick sections using a vibratome agarose. DAB revelation was performed by incubating floating sections with the DAB substrate (SIGMAFAST tablets, D4293-5SET, Sigma-Aldrich) for 20 min at RT. After 2 washes in 0.1 M cacodylate buffer, samples were post-fixed in 1% OsO<sub>4</sub>/1.5% ferrocyanide, dehydrated in ethanol and embedded into epoxy-resin (Agar 100 resin, Agar Scientific Ltd, UK). Ultrathin

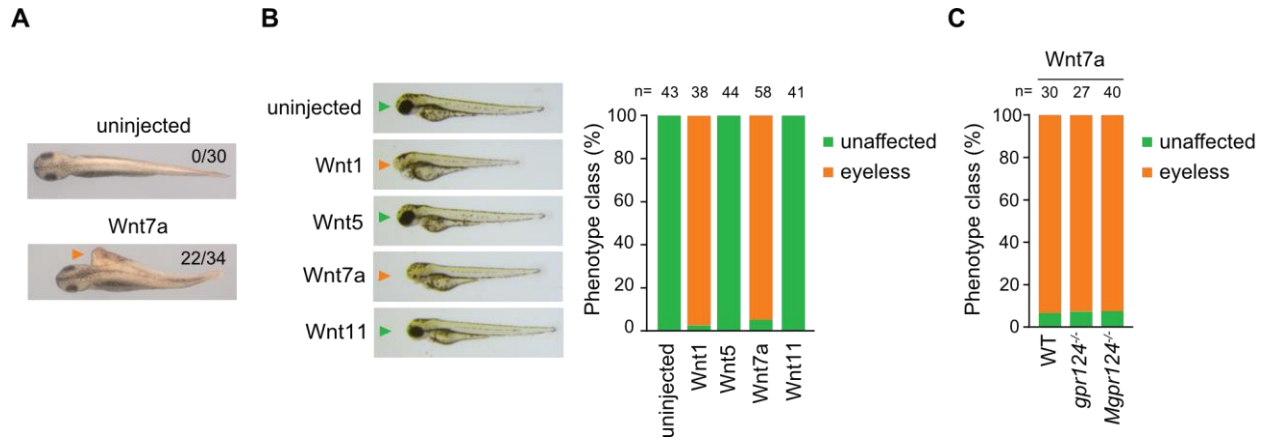
sections (70 nm) were collected and observed using a Tecnai10 TEM (FEI-Thermo Fisher). Images were captured with a Veleta CCD cam.

### ***Image acquisition and processing***

Images of cells, zebrafish embryos, and mouse brain slices were collected using an inverted laser scanning confocal microscope Zeiss LSM710 equipped with spectral PMT detector using 20X/0.8 dry and 63X/1.4 oil objectives and driven by Zen Blue controlling software. H&E and DAB-stained brain slices were imaged on a Leica stereoscope or on a wide-field Zeiss Axio Observer Z1 microscope. *Xenopus* larvae were imaged with an Olympus SZX16. We used ImageJ for image preparation (adjustments of levels and contrast, maximum intensity projections and sums and removal of outliers) and Imaris software (BitPlane) for the 3D representation of brain vasculature using wire diagrams. We used CellProfiler to analyze the RNAScope images. The hematoxylin-DAB stained images were deconvolved into two separate channel images (UnmixColors operation) and the objects of interest (nuclei and RNAScope spots) were separated from the background using an "A trous" wavelet filter (79) plugin we developed in-house (available at <https://github.com/zindy/libatrous>). With an appropriate filter and bandpass window (Lin3x3 kernel, scales 2-5), this plugin can separate the punctiliar RNAScope marker from the residual background in the DAB deconvolved channel. Spots are then detected as objects using a Primary Object Identification (IdentifyPrimaryObjects, Global Otsu) and their area was computed (MeasureObjectSizeShape).

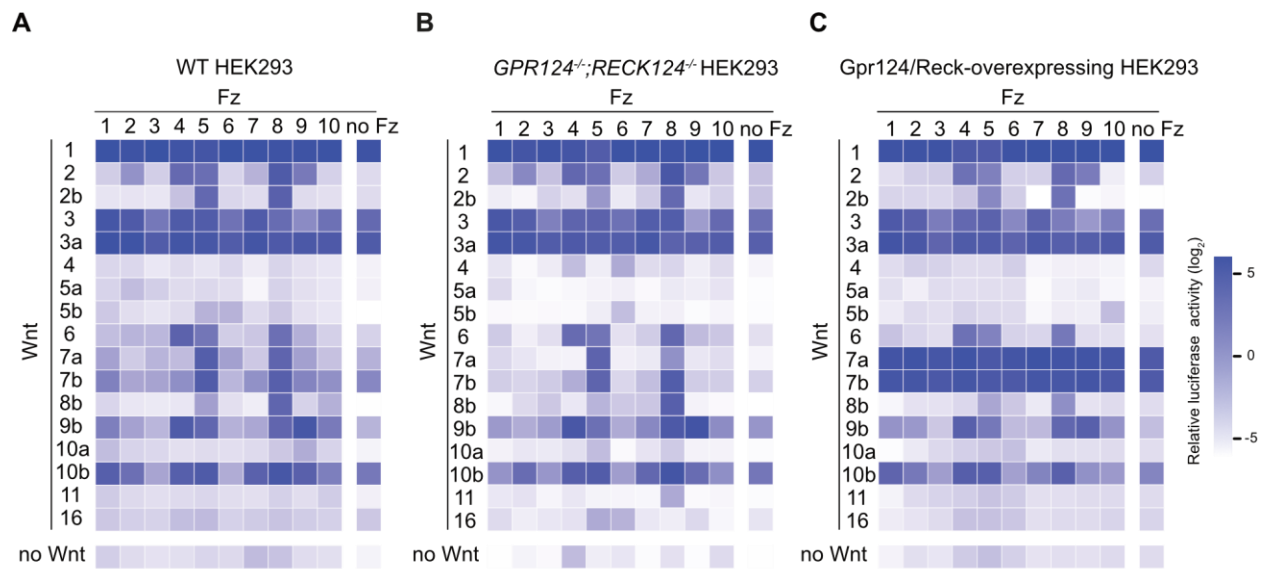
### ***Statistical analysis***

Statistical analysis was performed using GraphPad software. Data represent mean  $\pm$  SD. p-values were calculated by two-way ANOVA (fig. S14E), one-way ANOVA (with post hoc Dunnett's test, fig. 1B, 1E, fig. 2B, fig. 6C, fig. S3A, S3B, fig. 4B-D, fig. S13) and Student's t test (fig. S4C) for multiple and single comparisons of normally distributed data, respectively and by the Kruskal-Wallis (post hoc Dunn's test, fig. 3B-E, 3H, fig. 6B, 6E-G, fig. S9A, fig. S14A-D, fig. S19A-C) and Mann-Whitney test (fig. 4E, fig. 5A, 5C-G, fig. 6H-I) for multiple and single comparisons of non-normally distributed data, respectively. \*  $P < 0.05$ , \*\*  $P < 0.01$ , \*\*\*  $P < 0.001$ .



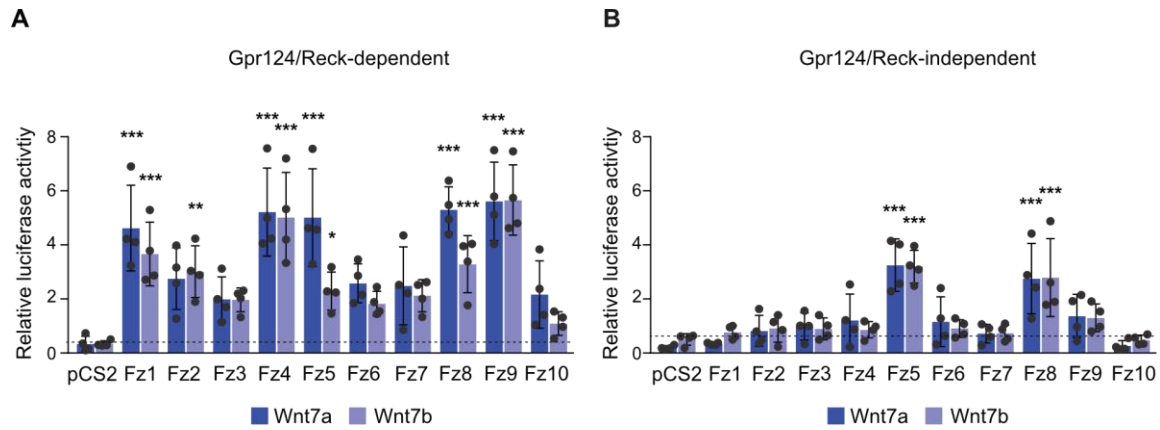
**Fig. S1. Developmental defects associated with Wnt7a expression in *Xenopus* and zebrafish**

(A) Phenotypic scoring of stage 36 *Xenopus laevis* embryos injected or not in the ventral vegetal region of the 4-cell embryo with 15 pg of Wnt7a mRNA. The orange arrowhead highlights axis duplication. Data for Wnt7a injection are the same as in Fig. 1F. (B) Gross morphology of 3 dpf WT zebrafish larvae injected at the one-cell stage with 20 pg mRNA of the indicated Wnt ligand. Wnt5 and Wnt11 are used as negative control “non-canonical” Wnt ligands. The percentage of embryos showing posteriorization of the anterior nervous system resulting in eye and forebrain loss (orange arrowhead) or not (unaffected, green arrowhead) are scored. (C) Phenotypic scoring of WT, *gpr124<sup>-/-</sup>* and maternal zygotic *gpr124<sup>-/-</sup>* (*Mgpr124<sup>-/-</sup>*) zebrafish larvae injected with 20pg of Wnt7a mRNA as in B.



**Fig. S2. Gene family-wide assessment of Gpr124/Reck impact on Wnt/Fz relationships**

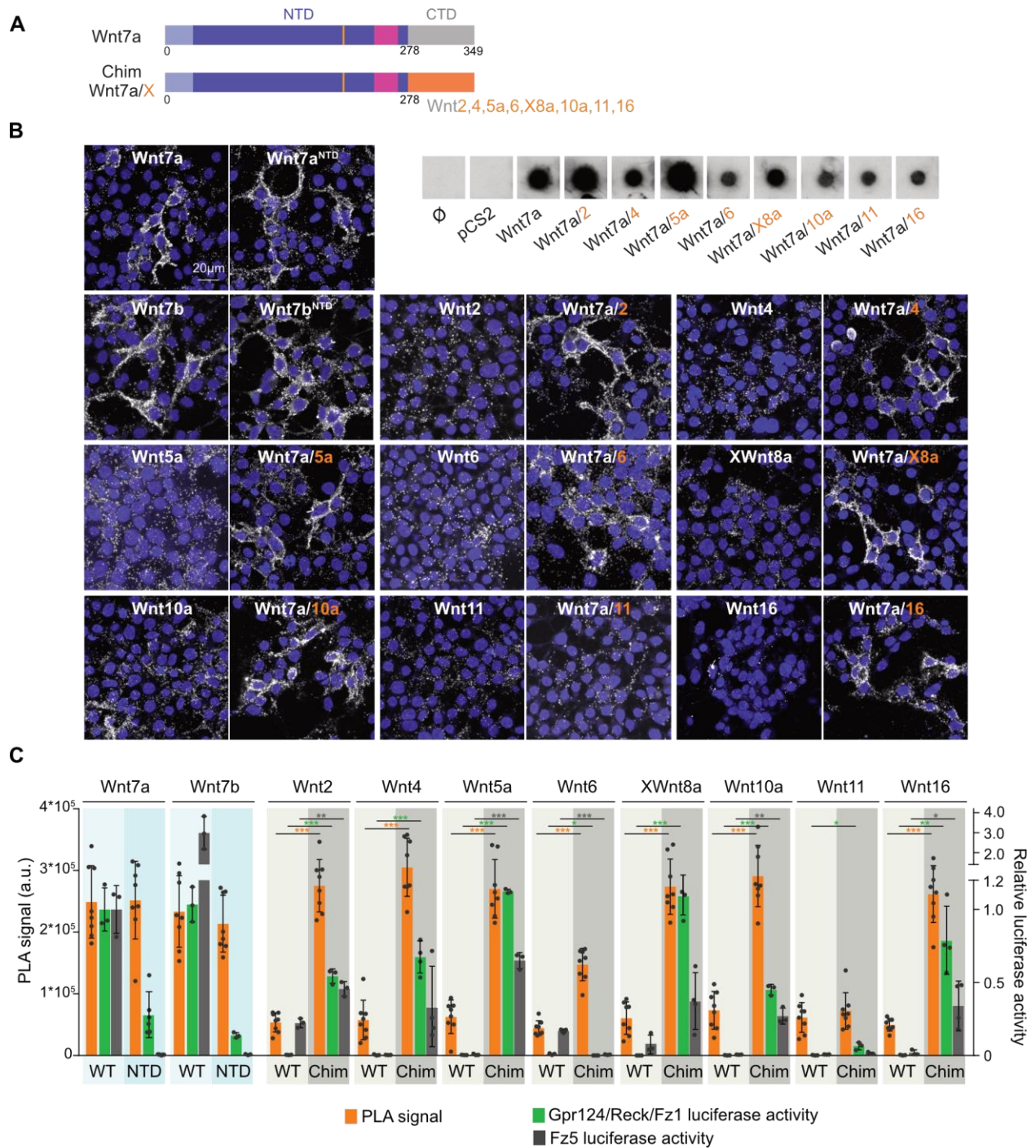
Heat map representation of average luciferase activities (n=3) 48 h after transfection of 17 of the 19 Wnt ligands in pairwise combination with each of the ten Fz receptors in WT (A), *GPR124*<sup>-/-</sup>; *RECK*<sup>-/-</sup> (B) and *Gpr124/Reck*-overexpressing HEK293 STF cells (C). For numerical values, see Table S1.



**Fig. S3. Frizzled specificity for Wnt7a/b signaling in the presence or absence of Gpr124/Reck**

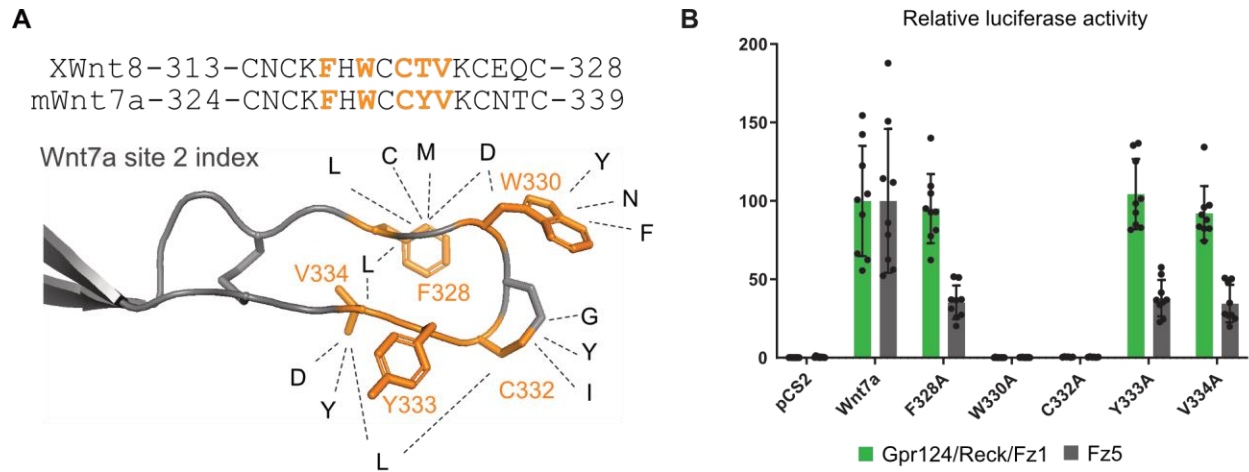
(A) Gpr124/Reck-dependent and (B) -independent STF luciferase activity in *GPR124*<sup>-/-</sup>;*RECK*<sup>-/-</sup>;*FZ1-10*<sup>-/-</sup> HEK293T cells after co-transfection of Wnt7a or Wnt7b with all 10 Fz genes or the empty pCS2 vector. \*P<0.05; \*\*P<0.01; \*\*\*P<0.001; data represent mean ± SD.





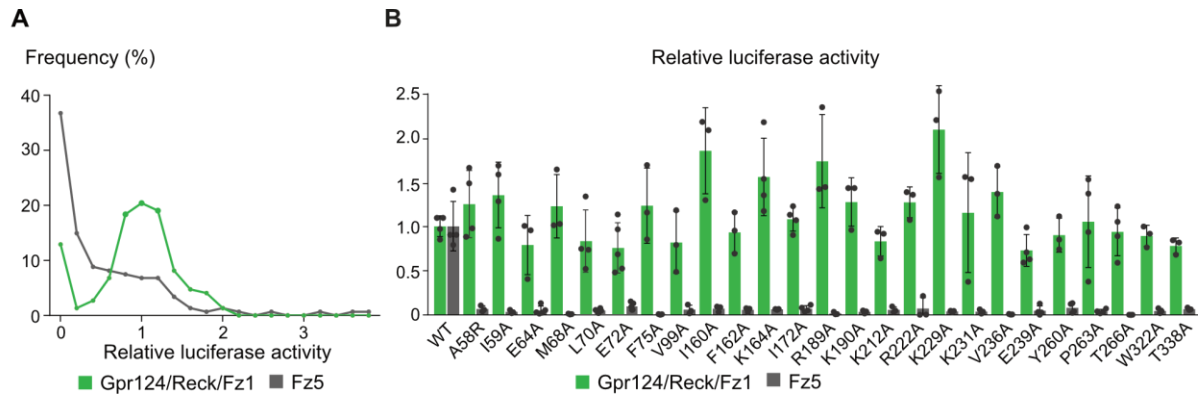
**Fig. S4. Chimeric Wnt7<sup>NTD</sup>/WntX<sup>CTD</sup> ligands mediate Gpr124/Reck-dependent signaling**

Chimeric V5-flagged constructs consisting of Wnt7a NTD and a CTD derived from other Wnts (A) were expressed together with HA-Reck in *GPR124*<sup>-/-</sup>;*RECK*<sup>-/-</sup> HEK293 cells and their secretion (dotplot, B, top right), Reck-associated PLA signal (B, C, orange bars) and STF relative luciferase activities in the presence of Gpr124/Reck/Fz1 (C, green bars) or Fz5 (C, grey bars) were assessed. Data for Wnt7a NTD are the same as in Fig. 1B. \**P*<0.05; \*\**P*<0.01; \*\*\**P*<0.001; data represent mean ± SD.



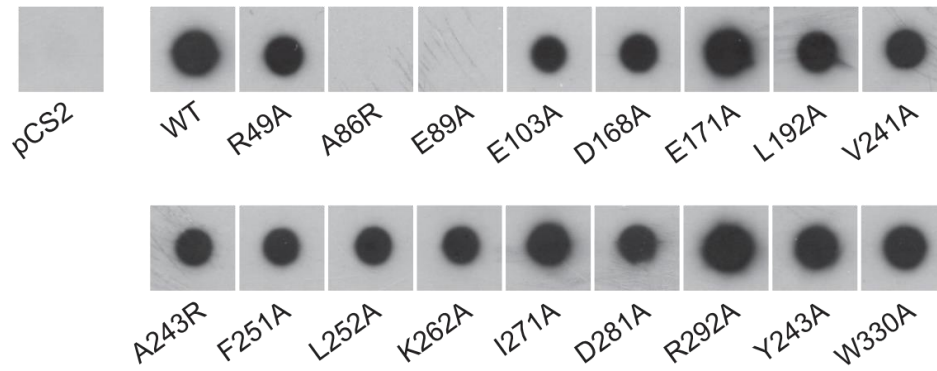
**Fig. S5. Beta-catenin signaling assay in STF cells of Wnt7a variants mutated for residues involved in the site 2 Wnt7a/Fz interaction**

Sequence alignment of *Xenopus* Wnt8 and mouse Wnt7a index (A, top) and structural model of Wnt7a based on the crystal coordinates of XWnt8a (20) (A, bottom). The orange Wnt7a residues predicted to be implicated in contacts with Fz residues (the predicted interacting amino acids of Fz5 or Fz8 are in black) within the site 2 interface were mutated to alanines. The relative STF luciferase activity of the corresponding variants was measured on Gpr124/Reck/Fz1 (green) or Fz5 (grey) (B). Data represent mean  $\pm$  SD.



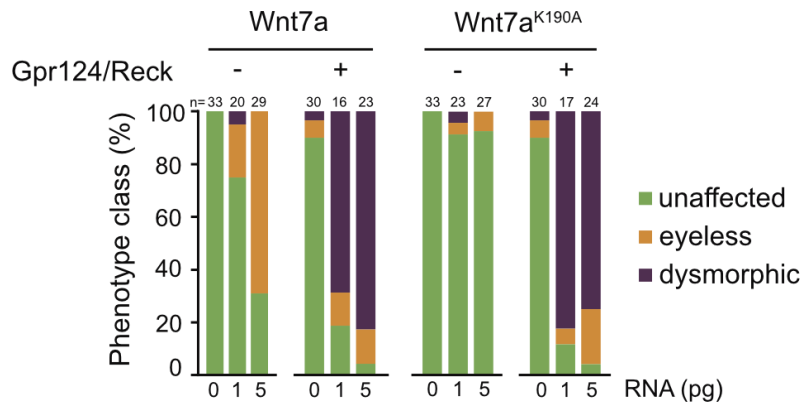
**Fig. S6. Beta-catenin signaling assay of single-residue Wnt7a variants in STF cells**

(A) Frequency distribution of the relative STF luciferase activity of the 147 Wnt7a variants on Gpr124/Reck/Fz1 (green) or Fz5 (grey) signaling. (B) Relative STF luciferase activity of Gpr124/Reck agonists on Gpr124/Reck/Fz1 (green) or Fz5 (grey). Data represent mean  $\pm$  SD.



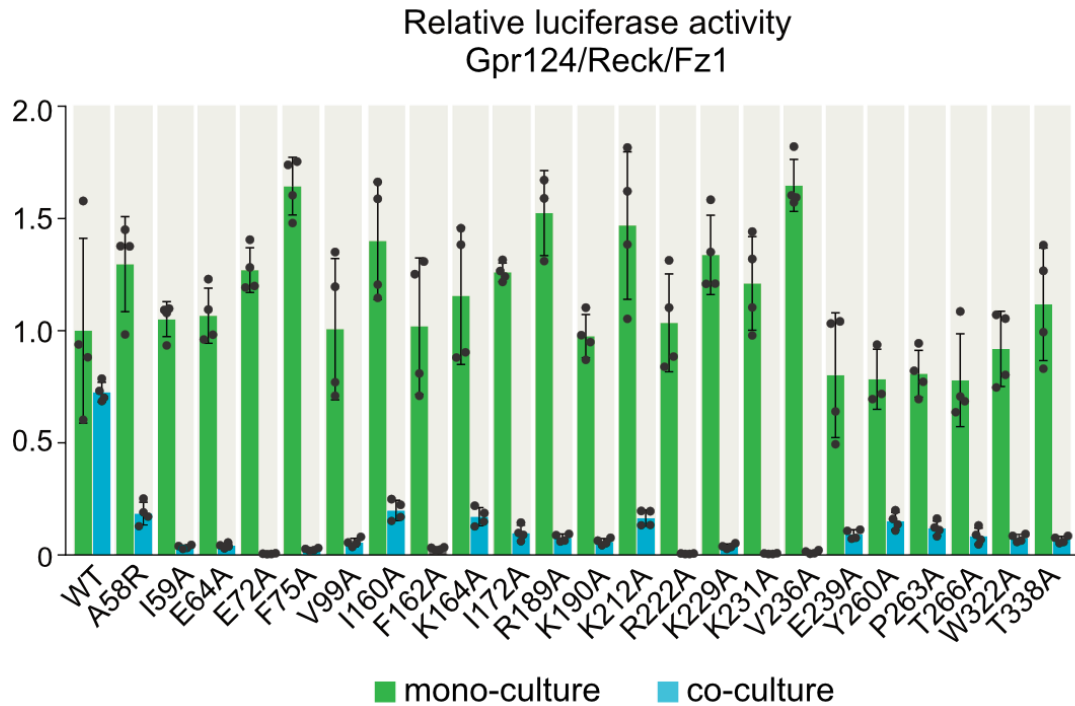
**Fig. S7. Anti-V5 dot blot analysis of Wnt7a variants secretion**

Ligand secretion was evaluated qualitatively by means of anti-V5 dot blot analysis of HEK293T cellular supernatants collected 48 h after transfection with WT Wnt7a or the indicated signaling inactive Wnt7a variants. Only A86R and E89A were not detected in the supernatant.



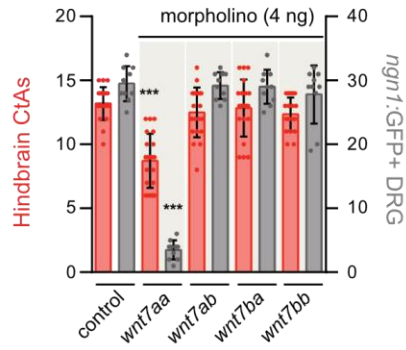
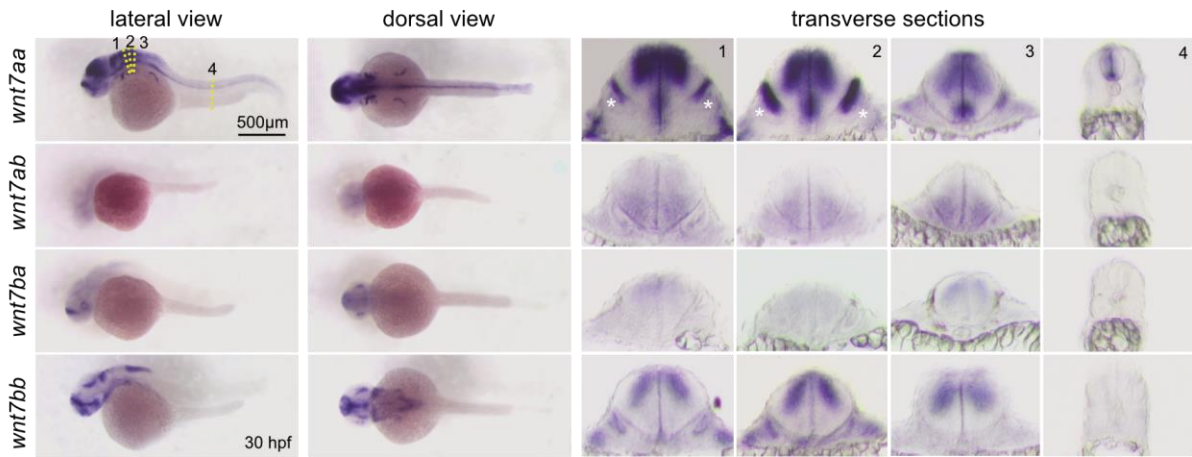
**Fig. S8. Morphological defects induced by injection of low mRNA doses of Wnt7a or Wnt7a<sup>K190A</sup> in zebrafish embryos after ubiquitous expression of Gpr124/Reck**

Phenotypic scoring of 3 dpf zebrafish larvae injected at the one-cell stage with Wnt7a or Wnt7a<sup>K190A</sup> mRNA at the indicated doses, in combination or not with 100 pg of Reck and Gpr124 mRNA.



**Fig. S9. Autocrine versus paracrine activity of the Gpr124/Reck agonists**

Relative Gpr124/Reck/Fz1-dependent STF luciferase activity of the Gpr124/Reck agonists in mono-culture (autocrine, green) and co-culture settings (paracrine, blue) as described in Fig. 2F. Wnt7a variants are either secreted by the reporter cells (mono-culture) or by a population of co-cultured cells (1:1). Data represent mean  $\pm$  SD.

**A****B**

**Fig. S10. Functional and gene expression analysis of the zebrafish *wnt7a/b* paralogues**

(A) Quantification of 60 hpf *Tg(kdrl:GFP)* hindbrain CtAs and 72 hpf *Tg(neurog1:GFP)* trunk DRG in the indicated zebrafish *wnt7* morphants (4 ng each). (B) Lateral and dorsal bright-field images of whole-mount in situ hybridization for *wnt7aa*, *wnt7ab*, *wnt7ba* and *wnt7bb* in 30 hpf WT embryos. (Right) transverse sections of the hindbrain and the trunk taken at levels indicated on the left. The otic vesicles are marked by an asterisk.

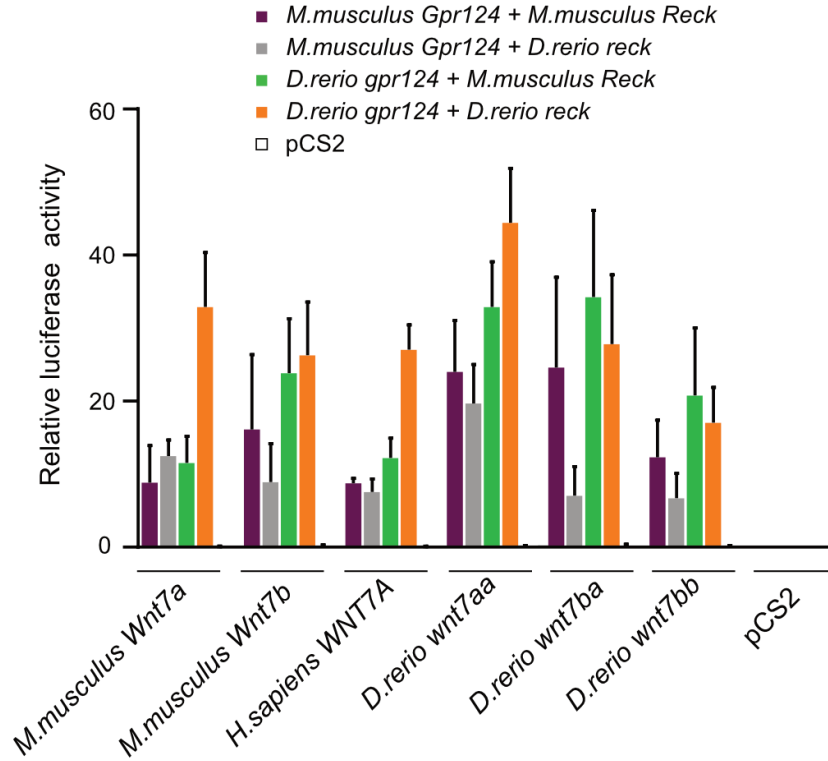
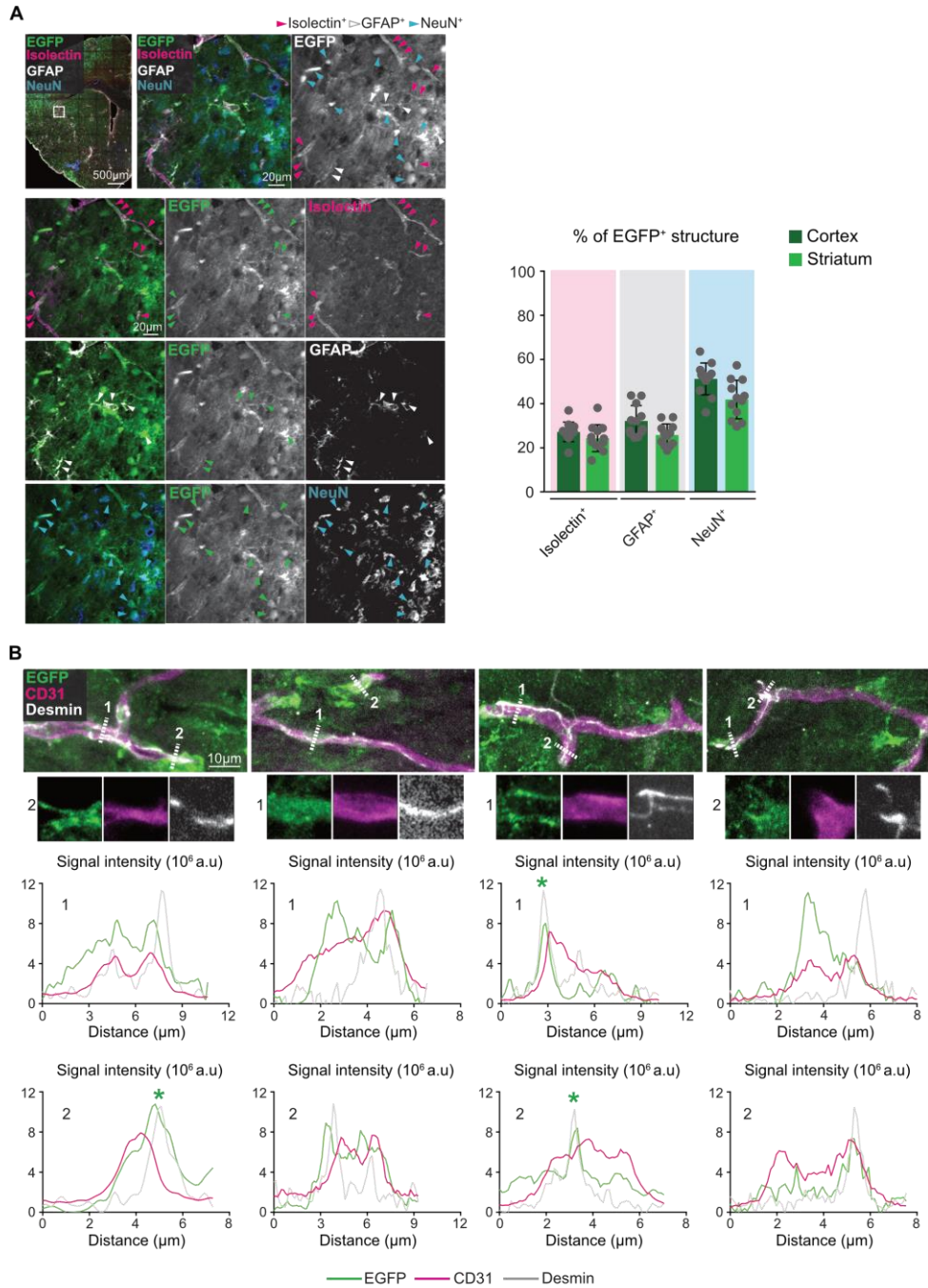


**Fig. S11. Evolutionary cross-reactivity of Wnt7a/b, Reck and Gpr124**

Relative luciferase activity of HEK293 STF cells after co-transfection with different mouse, human, or zebrafish Wnt7 isoforms in combination with orthologues of murine or zebrafish Gpr124 and Reck. Data represent mean  $\pm$  SD.





Martin et al., Figure S12

**Fig. S12. Cellular origins of  $\text{Wnt7a}^{\text{K190A}}$  upon AAV-PHP.eB gene delivery**

Two weeks after intravenous injection of  $4.10^{11}$  vg of AAV-PHP.eB-CAG- $\text{Wnt7a}^{\text{K190A}}$ -P2A-EGFP, EGFP (green) was co-immunostained with (A) endothelial cells (isolectin, magenta), astrocytes (GFAP, white) and neurons (NeuN, cyan) or (B) endothelial cells (CD31, magenta) and pericytes (Desmin, white). For pericyte co-localization assessment, three-color-intensity profiles along a line were made using the ‘plot profile’ option in ImageJ for each channel (EGFP, Desmin, CD31). The asterisks in the profiles below indicate presumptive colocalization between the EGFP and Desmin. Data represent mean  $\pm$  SD.

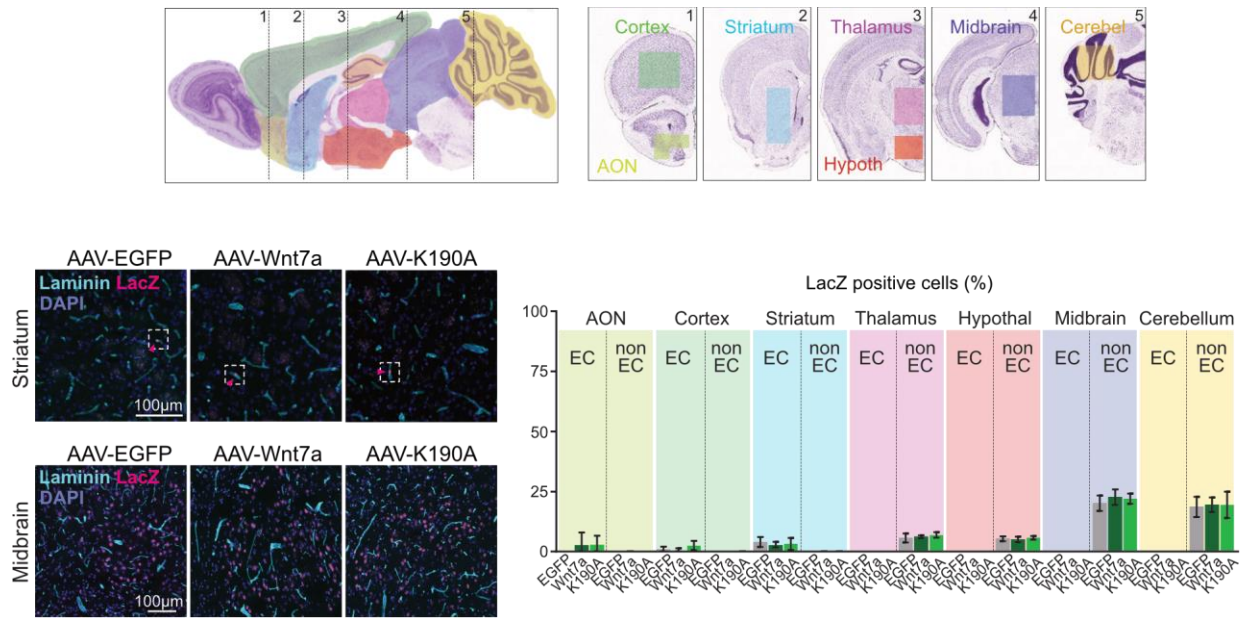


**Fig. S13. Brain-wide analysis of Wnt activation after AAV-PHP.eB gene delivery of Wnt7a or Wnt7a<sup>K190A</sup> in BAT-GAL mice**

At 8 weeks of age, BAT-GAL mice were injected retro-orbitally with  $4 \cdot 10^{11}$  vg (viral genomes) of the indicated AAV viruses. After two weeks, coronal brain slices were stained for lacZ (magenta), laminin (cyan), and DNA (DAPI, blue). The percentage of LacZ<sup>+</sup> endothelial cells (ECs) and non-endothelial cells (non-ECs) in different brain regions is plotted on the right. AON, Anterior Olfactory Nucleus. Data represent mean  $\pm$  SD.

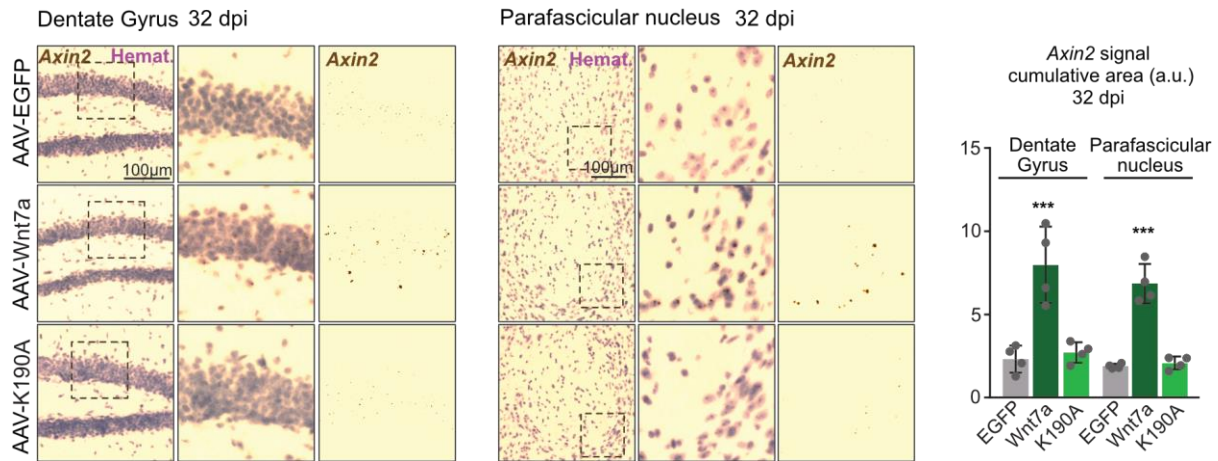


**Fig. S14. Absence of ectopic Wnt activation after brain-wide Wnt7a<sup>K190A</sup> gene delivery**

At 8 weeks of age, WT C57BL6 mice were injected retro-orbitally with  $4 \cdot 10^{11}$  vg (viral genomes) of the indicated AAV viruses. 32 days after viral injection, RNAScope *in situ* hybridization of *Axin2* was performed in coronal sections of the hippocampal dentate gyrus and the parafascicular nucleus of the thalamus. The RNAScope images were analyzed using CellProfiler as described in the Methods section. \*\*\* $P < 0.001$ ; data represent mean  $\pm$  SD.

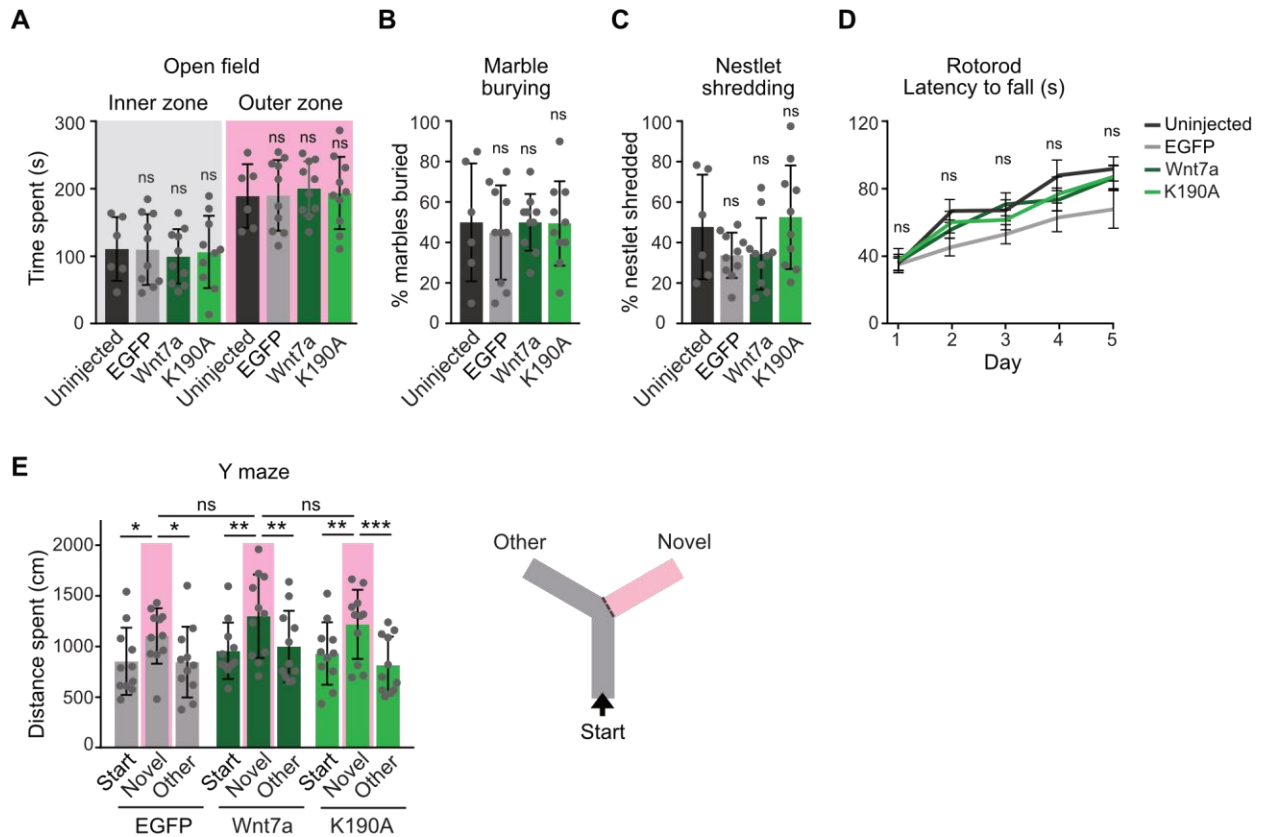


**Fig. S15. Behavioral assays of AAV-PHP.eB-injected adult mice**

At 8 weeks of age, male C57BL6 mice were injected retro-orbitally with  $4.10^{11}$  vg (viral genomes) of the indicated AAV viruses. Three weeks after viral injection, mice were tested in the open field (A), marble burying (B), nestlet shredding (C) rotarod (D), and Y-Maze (E) behavioral assays along with a group of uninjected control mice as described in the Methods section. \* $P < 0.05$ ; \*\* $P < 0.01$ ; \*\*\* $P < 0.001$ ; data represent mean  $\pm$  SD.

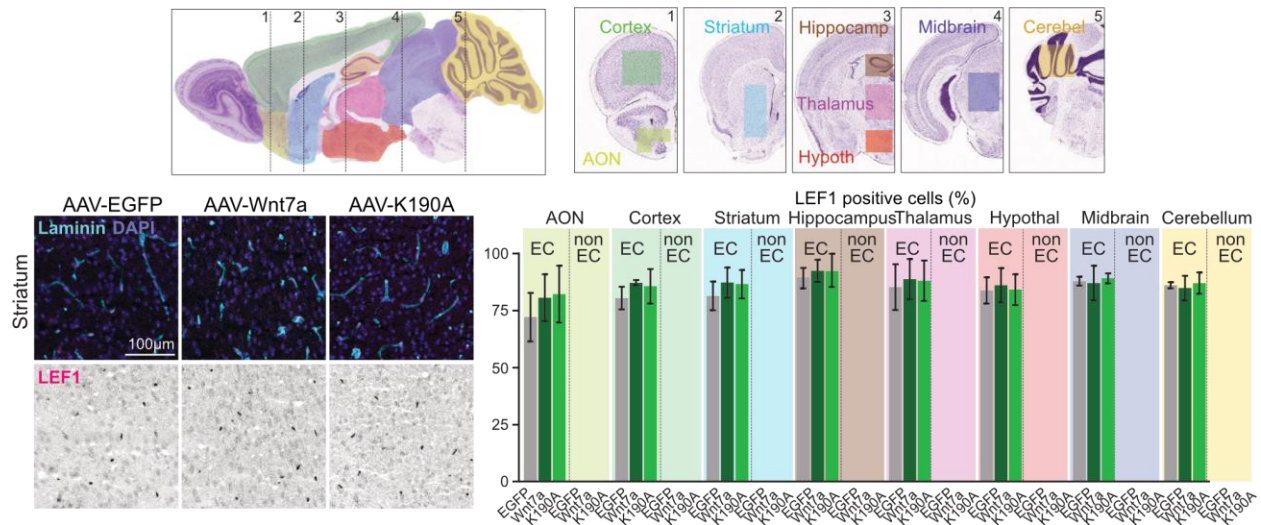
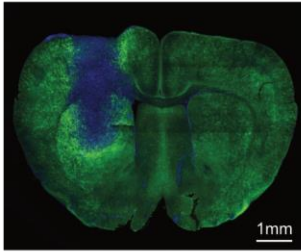


**Fig. S16. LEF1 immunostaining after brain-wide Wnt7a or Wnt7a<sup>K190A</sup> gene delivery**

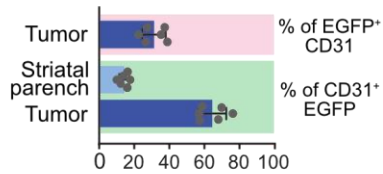
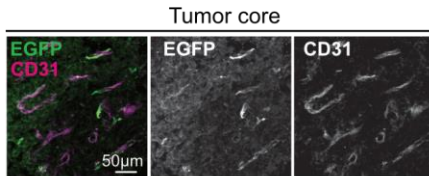
At 8 weeks of age, WT C57BL6 mice were injected retro-orbitally with  $4.10^{11}$  vg (viral genomes) of the indicated AAV viruses. 14 days after viral injection, LEF1 immunostaining (magenta, grey) was performed to assess Wnt activation in endothelial cells (ECs, laminin, cyan) and non-endothelial cells (non-ECs). The percentage of LEF1<sup>+</sup> cells in different brain regions is plotted on the right. AON, Anterior Olfactory Nucleus. Data represent mean  $\pm$  SD.



A



B



C

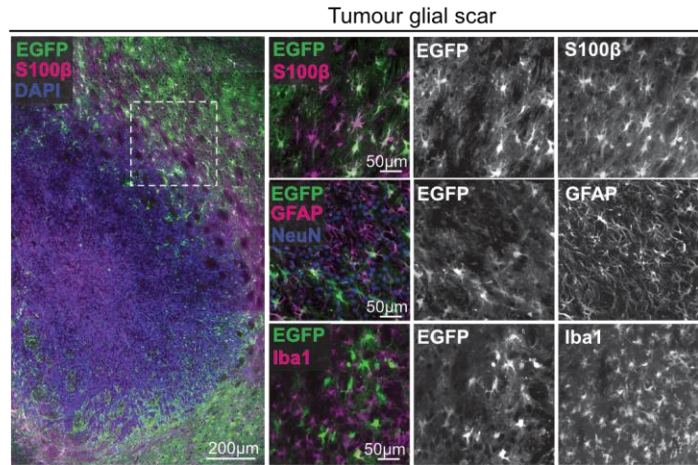


**Fig. S17. Distribution of Wnt7a<sup>K190A</sup>-releasing EGFP<sup>+</sup> cells in and around GL261 tumors after AAV-PHP.eB gene delivery**

(A) Confocal tile scan of a coronal section through a GL261 glioblastoma tumor developing in a AAV-PHP.eB-CAG-Wnt7a<sup>K190A</sup>-P2A-EGFP injected mice 24 days post implantation. GL261 cells, readily labeled by DAPI, are negative for the EGFP viral transduction marker, which is particularly high at the tumor margin. (B) anti-EGFP (green, white) and anti-CD31 (endothelial cells, magenta, white) immunostaining within the core of the tumor. (C) Immunostaining of EGFP (viral transduction marker, green, white), S100 $\beta$  (astrocytes, magenta, white), GFAP (astrocytes, magenta, white), NeuN (neurons, blue, white), Iba1 (microglial cells, magenta, white) within the tumor glial scar.

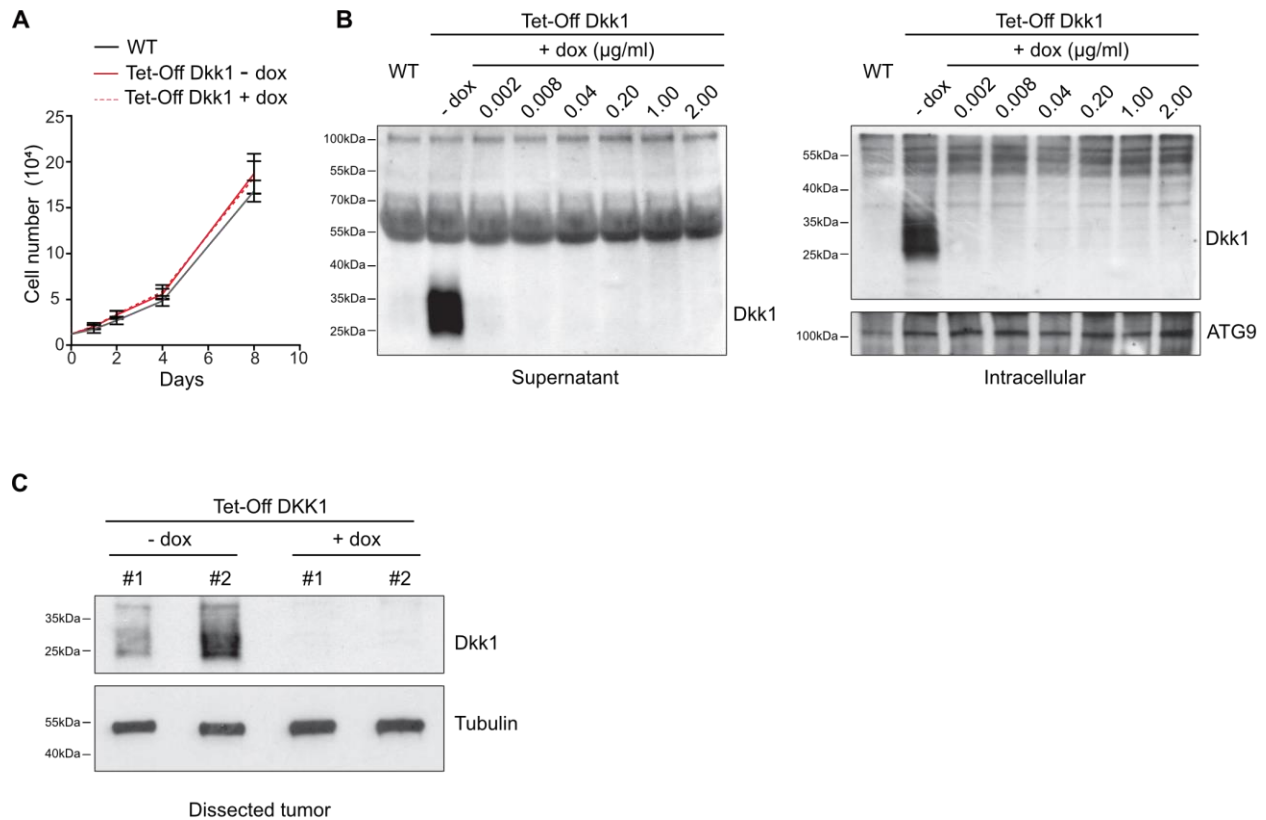


**Fig. S18. *In vitro* and *in vivo* characterization of the Tet-Off Dkk1 GL261 cell line**

(A) Growth curve of WT GL261 cells and Tet-Off Dkk1 GL261 cells exposed or not to 1  $\mu\text{g}\cdot\text{ml}^{-1}$  doxycycline (B) Western blot analysis of conditional Dkk1 repression addition of doxycycline to the growth medium for 48 h. Dkk1 was probed both in the cellular supernatant (left) and the cells (right). ATG9 is used as a loading control for the cellular extracts. (C) Western blot analysis of Dkk1 expression within tumors at 21 days post implantation in mice fed or not with a doxycycline-containing diet as described in the Methods section. Two independent tumors are shown for each condition. Tubulin is used as loading control.

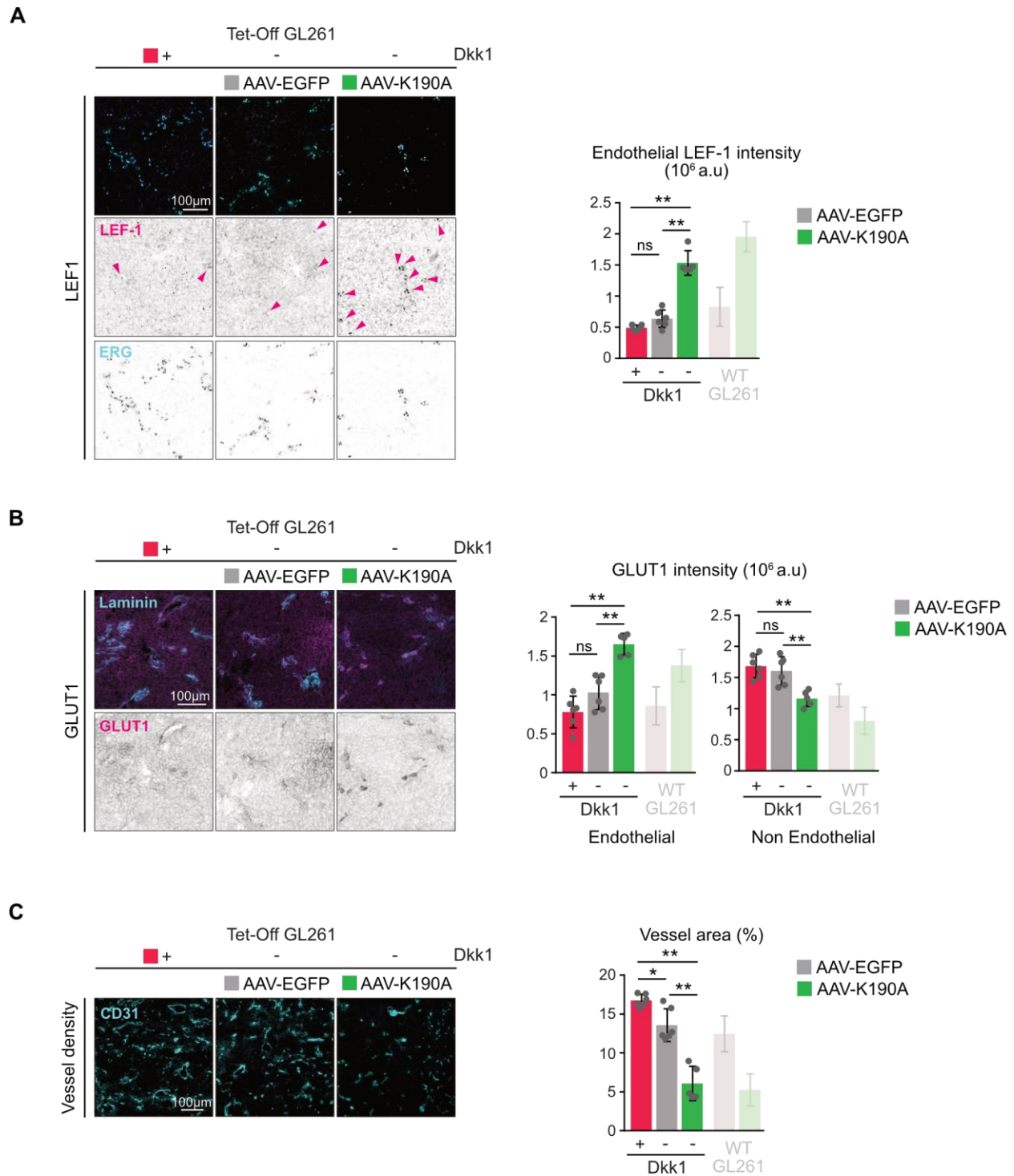


**Fig. S19. *In vivo* characterization of the Tet-Off Dkk1 GL261 tumors**

(A) Co-immunostaining of coronal tumor sections for LEF1 (magenta) together with the endothelial nuclear marker ERG (cyan) (B) GLUT1 (magenta, grey) together with laminin (cyan) and (C) endothelial cells (CD31, cyan). Quantifications were done as described in Fig. 5 and data for WT GL261 (in transparency) are the same as in Fig. 5C, E, F.



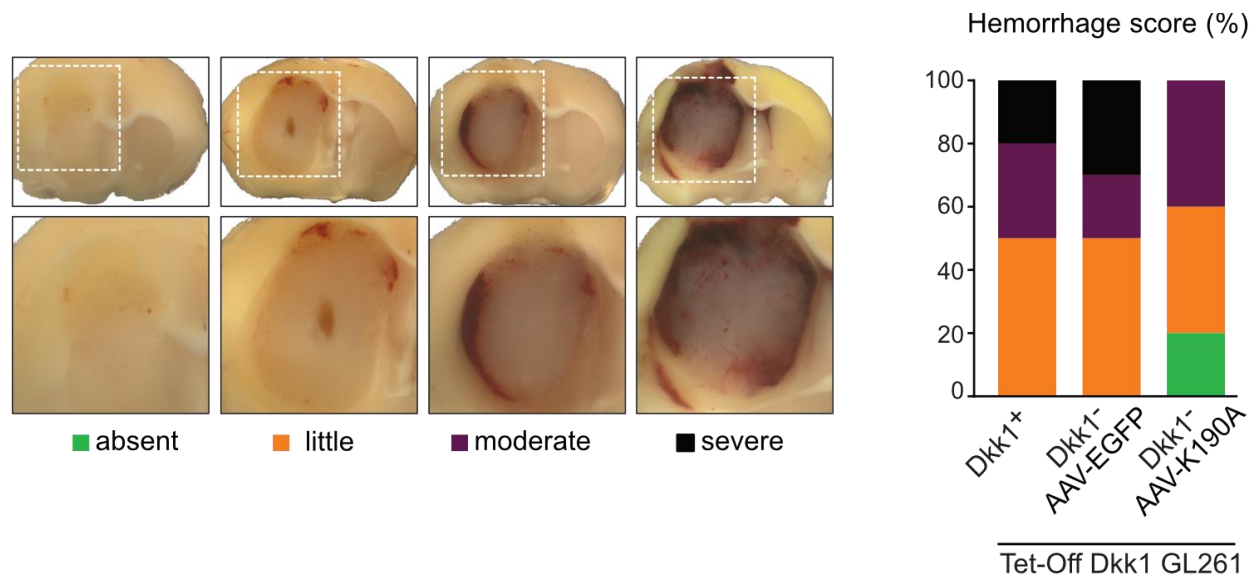


**Fig. S20. Hemorrhage score of Tet-Off Dkk1 tumors after AAV-EGFP or AAV-K190A gene delivery**

At 25 days post implantation of  $1.10^5$  Tet-Off Dkk1 GL261 cells, brains were harvested from mice injected or not with the indicated AAV virus. Intra- and peritumoral hemorrhages were categorized on vibratome sections as shown on the left, and scored in a double-blind manner.

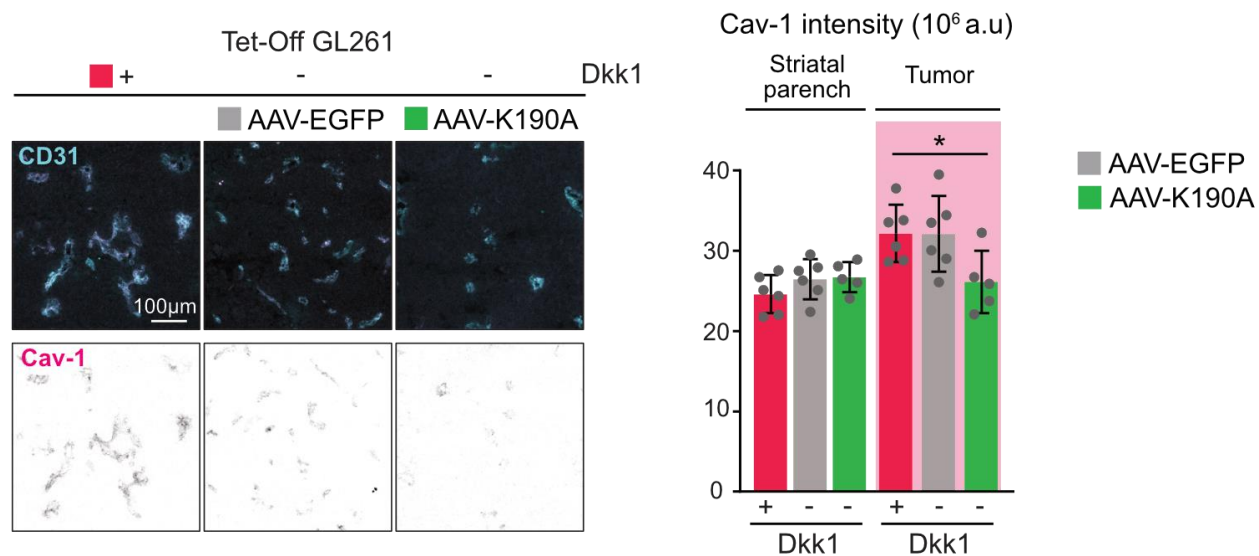


**Fig. S21. Caveolin-1 immunostaining in Tet-Off Dkk1 GL261 tumors**

Co-immunostaining of endothelial cells (CD31, cyan) and Caveolin-1 (magenta, grey) in Tet-Off Dkk1 GL261 tumors harvested from mice injected or not with the indicated AAV virus.

\*P<0.05; data represent mean  $\pm$  SD.



**Table S1. Gene family-wide assessment of Gpr124/Reck impact on Wnt/Fz relationships**

Relative luciferase activity 48 h after transfection of 17 of the 19 Wnt ligands in pairwise combination with each of the ten Fz receptors in WT (top), *GPR124*<sup>-/-</sup>;*RECK*<sup>-/-</sup> (middle) and Gpr124/Reck-overexpressing HEK293 STF cells (bottom). For each pairwise Fz/Wnt combination, the relative Firefly/Renilla luciferase activities were determined in triplicate. The heat map of Figure 1 is the representation of the average of these three results on a log scale.



	Gpr124/Reck /Fz1		Fz5			Gpr124/Reck /Fz1		Fz5			Gpr124/Reck /Fz1		Fz5	
	mean	SD	mean	SD		mean	SD	mean	SD		mean	SD	mean	SD
G33A	1.23	0.51	0.68	0.38	R143A	1.39	0.26	1.24	0.22	P249A	1.10	0.35	0.10	0.02
I36A	0.97	0.54	1.28	0.19	D144A	1.31	0.35	0.99	0.04	P250A	1.28	0.35	1.28	0.29
I37A	0.05	0.06	0.58	0.18	E145A	1.09	0.17	0.85	0.29	F251A	0.06	0.02	0.04	0.03
K40A	0.79	0.33	1.93	0.90	K148A	0.87	0.25	0.97	0.53	L252A	0.00	0.00	0.03	0.03
I41A	1.78	0.53	0.76	0.31	D155A	0.58	0.23	0.39	0.19	K253A	0.52	0.25	0.02	0.01
P42A	1.22	0.67	0.82	0.15	R157A	1.35	0.15	0.80	0.07	I254A	0.54	0.10	0.08	0.05
L44A	0.04	0.06	0.05	0.06	Y158A	1.76	0.58	0.55	0.18	K255A	1.08	0.35	2.53	0.39
R47A	0.84	0.34	1.34	0.58	<b>I160A</b>	1.85	0.48	0.07	0.03	K256A	0.90	0.25	1.43	0.54
R49A	0.08	0.06	0.02	0.01	<b>F162A</b>	0.93	0.23	0.06	0.02	P257A	1.14	0.88	0.19	0.16
A50R	0.94	0.42	0.35	0.26	<b>K164A</b>	1.55	0.44	0.06	0.01	L258A	1.07	0.54	1.14	0.65
S54A	1.18	0.28	0.64	0.30	F166A	0.60	0.13	0.04	0.01	S259A	0.76	0.33	0.48	0.37
R55A	0.57	0.17	1.02	0.32	D168A	0.00	0.00	0.01	0.01	<b>Y260A</b>	0.90	0.19	0.08	0.06
D57A	1.15	0.24	0.32	0.13	R170A	1.09	0.19	2.29	0.68	R261A	1.08	0.55	0.13	0.08
<b>A58R</b>	1.25	0.38	0.07	0.03	E171A	0.02	0.01	0.03	0.02	K262A	0.00	0.00	0.02	0.01
<b>I59A</b>	1.13	0.59	0.05	0.03	<b>I172A</b>	1.08	0.14	0.07	0.03	<b>P263A</b>	1.05	0.51	0.04	0.02
I60A	0.83	0.09	1.04	0.44	K173A	1.06	0.18	0.94	0.30	M264A	1.21	0.37	1.25	0.25
V61A	1.26	0.47	1.89	1.65	A176R	0.43	0.25	0.12	0.16	D265A	1.02	0.22	1.20	0.60
I62A	0.99	0.26	0.42	0.11	R177A	0.40	0.03	0.01	0.01	<b>T266A</b>	0.94	0.27	0.00	0.00
G63A	0.84	0.13	0.95	0.18	E186A	1.69	0.26	0.29	0.13	D267A	0.93	0.18	0.12	0.20
<b>E64A</b>	0.79	0.33	0.05	0.05	<b>R189A</b>	1.73	0.53	0.02	0.02	I271A	0.01	0.01	0.01	0.01
S66A	1.15	0.07	0.88	0.10	<b>K190A</b>	1.27	0.27	0.04	0.02	E272A	0.96	0.49	0.16	0.07
<b>M68A</b>	0.83	0.35	0.05	0.02	L192A	0.01	0.01	0.03	0.01	K273A	1.15	0.51	3.75	0.92
<b>L70A</b>	0.75	0.29	0.09	0.04	E193A	1.27	0.55	1.33	0.34	E279A	0.33	0.16	0.02	0.01
D71A	1.07	0.55	0.72	0.29	E194A	1.58	0.16	0.47	0.32	E280A	0.90	0.29	0.77	0.22
<b>E72A</b>	1.22	0.36	0.01	0.00	K197A	1.71	0.52	0.20	0.09	D281A	0.00	0.00	0.03	0.03
Q74A	1.08	0.10	1.09	0.07	E199A	1.20	0.63	1.26	0.44	V287A	1.68	1.01	0.67	0.12
<b>F75A</b>	1.23	0.42	0.01	0.00	K201A	1.09	0.50	0.10	0.02	K296A	1.25	0.29	3.56	0.61
R78A	0.72	0.26	0.24	0.18	V205A	1.44	0.29	0.52	0.23	D305A	0.89	0.34	0.23	0.15
G80A	1.24	0.15	1.44	0.36	<b>K212A</b>	0.83	0.17	0.06	0.03	L306A	0.81	0.42	1.07	0.21
R81A	0.54	0.20	0.03	0.01	T216A	0.93	0.47	0.38	0.25	R311A	0.22	0.14	0.02	0.02
A86R	0.01	0.01	0.01	0.01	<b>R222A</b>	1.27	0.17	0.07	0.12	Y313A	0.09	0.04	0.03	0.04
E89A	0.00	0.00	0.01	0.00	E223A	1.89	0.04	1.16	0.59	Y318A	0.78	0.40	0.65	0.12
R90A	1.34	0.85	1.69	0.36	Y226A	1.34	0.13	0.22	0.09	R320A	0.59	0.10	0.07	0.02
T91A	0.55	0.31	0.19	0.09	V227A	1.23	0.23	0.46	0.12	V321A	1.29	0.23	0.44	0.05
V92A	2.01	0.88	0.45	0.22	<b>K229A</b>	2.09	0.49	0.04	0.01	<b>W322A</b>	0.89	0.12	0.05	0.03
F93A	0.17	0.09	0.01	0.02	D230A	0.91	0.02	0.87	0.39	K327A	1.14	0.44	1.30	0.61
K95A	1.32	0.55	3.12	1.17	<b>K231A</b>	1.15	0.67	0.04	0.02	F328A	0.05	0.04	0.66	0.50
E96A	1.05	0.25	0.70	1.01	E234A	1.47	0.30	0.92	0.29	H329A	0.94	0.19	1.39	0.41
K98A	1.17	0.30	0.24	0.05	<b>V236A</b>	1.38	0.29	0.01	0.00	W330A	0.00	0.00	0.07	0.05
<b>V99A</b>	0.82	0.35	0.06	0.05	<b>E239A</b>	0.73	0.18	0.05	0.05	Y333A	0.82	0.24	0.43	0.34
R102A	1.61	0.01	0.27	0.02	P240A	1.24	0.26	0.51	0.21	V334A	0.72	0.26	0.54	0.23
E103A	0.01	0.01	0.04	0.02	V241A	0.01	0.00	0.02	0.02	N337A	0.94	0.48	1.16	0.44
A121R	1.00	0.32	1.56	0.17	R242A	1.25	0.35	1.92	0.43	<b>T338A</b>	0.78	0.09	0.07	0.01
D130A	1.51	0.51	0.46	0.13	A243R	0.05	0.03	0.00	0.00	E341A	0.80	0.29	0.18	0.04
D134A	1.35	0.19	0.79	0.20	S244A	1.43	0.86	0.84	0.26	R342A	1.03	0.18	0.86	0.32
K135A	0.87	0.18	0.30	0.13	R245A	0.37	0.26	0.05	0.06	E344A	0.82	0.33	0.16	0.15
E136A	0.81	0.24	1.08	0.54	N246A	1.01	0.52	0.42	0.24	M345A	1.58	0.07	0.21	0.03
K137A	1.40	0.43	0.26	0.06	K247A	0.57	0.26	0.06	0.02	Y346A	0.95	0.40	0.27	0.21
Y141A	0.95	0.28	0.29	0.23	R248A	1.15	0.35	0.63	0.12	K349A	0.56	0.35	0.02	0.03
					<b>pCS2</b>	0.00	0.00	0.02	0.00					
					<b>Wnt7a</b>	1.00	0.18	1.05	0.16					
					XWnt8a	0.05	0.01	0.10	0.06					

**Table S2. Beta-catenin signaling assay using STF cells transfected with Gpr124/Reck/Fz1 or Fz5, together with the indicated Wnt7a single-residue variant.**

Relative luciferase activity 48 h after transfection of 147 single-residue variants of mouse Wnt7a together with Gpr124/Reck/Fz1 or Fz5 in HEK293 STF cells. For each variant, the mean luciferase activities were determined from three to five independent experiments (each conducted in triplicate technical replicates). Gpr124/Reck agonists are highlighted in blue, the empty pCS2 vector in red, and Wnt7a, used for normalization, in green.